

**MODELLING THE DAMAGE FORMATION OF
BOLTED CARBON FIBER REINFORCED EPOXY
COMPOSITE JOINTS AT INCREASING STRAIN
RATES**

**A Thesis Submitted to
the Graduate School of
İzmir Institute of Technology
in Partial Fulfillment of the Requirements for the Degree of**

MASTER OF SCIENCE

in Mechanical Engineering

**by
Çağatay ALBİR**

**June 2021
İZMİR**

ACKNOWLEDGMENTS

I would like to thank my supervisor Prof. Dr. Mustafa GÜDEN for his patience, endless support and encouraging approach during the entire thesis study. His guidance and expertise helped me to complete my thesis.

I would like to thank all the members of Dynamic Testing and Modelling Laboratory; Mustafa Kemal SARIKAYA, Mesut BAYHAN, Alican T. ALPKAYA, Burak HIZLI, Muhammet ÇELİK, Ozan BALYA and Berika YORULMAZLAR for their collaboration and support.

Last but not least, I would like to express my most sincere gratitude to my family, my father Ali ALBİR and my mother Dilek ALBİR for their endless support. This accomplishment would not have been possible without them.

ABSTRACT

MODELLING THE DAMAGE FORMATION OF BOLTED CARBON FIBER REINFORCED EPOXY COMPOSITE JOINTS AT INCREASING STRAIN RATES

The bearing strength of a carbon fiber reinforced/epoxy unidirectional composite joint incorporating a single hex bolt fastener was investigated under quasi-static and dynamic loads experimentally and numerically with two different bolt torques, 2.5 N m and 10 N m. The tests were conducted with neat fit clearance and without washer. The quasi-static tests were conducted at 3.33×10^{-5} and $1.66 \times 10^{-3} \text{ m s}^{-1}$ according to the ASTM D5961 Procedure C. The dynamic tests were conducted in at Tension Split Hopkinson Pressure Bar (TSHPB) at 12.68 m s^{-1} using a specially designed specimen grip to ensure the same conditions as the quasi-static tests. Three dimensional explicit finite element models of bearing tests were developed in the LS-DYNA and the composite was modelled using the MAT_162 composite material model incorporating the strain rate effects. At the quasi-static velocities, a relatively low strain rate dependence of bearing peak force was found with almost no effect of applied bolt torque. In the TSHPB tests, the bearing force increased by 57% of those of quasi-static tests. The deformation mode also altered in dynamic tests and the increase of the bolt torque resulted with increasing the bearing peak force by 5%.

ÖZET

ARTAN GERİNİM HIZLARINDA VİDA BAĞLANTILI KARBON FİBER TAKVİYELİ EPOKSİ KOMPOZİTLERDE HASAR OLUŞUMUNUN MODELLENMESİ

Tek bir altıgen civata bağlantı elemanı içeren tek yönlü kompozit bağlantılarının mekanik davranışı hem deneysel hem de sayısal olarak 2.5 Nm ve 10 Nm'lik iki farklı civata torku ile yarı statik ve dinamik yükleme koşulları altında incelendi. Testler sıkı geçme, 3'lük sabit E/D oranı, 6'lık sabit W/D oranı ile rondelasız olarak gerçekleştirildi. Yarı statik testler Prosedür C'ye göre 3.33×10^{-5} ve $1.66 \times 10^{-3} \text{ m s}^{-1}$ olmak üzere iki farklı yükleme hızında gerçekleştirildi. Dinamik testler TSHPB (Tension Split Hopkinson Pressure Bar) ile yarı statik testlerle aynı koşulları sağlamak için iki adet aparat kullanılarak 12.68 m s^{-1} yükleme hızında gerçekleştirildi. Test edilen numunelerin üç boyutlu sonlu elemanlar modelleri LS-DYNA yazılımı kullanılarak geliştirildi ve kompozit malzemeyi modellemek için gerinime bağlı malzeme modeli Mat_162 kullanıldı. Yarı statik yükleme aralığında, nihai kırılma kuvveti açısından nispeten düşük gerinim hızı bağımlılığı gözlemlendi ve civata torkundaki artışın neredeyse hiçbir etkisi olmadı. Dinamik yükleme hızında, yarı statik testlere kıyasla nihai kırılma kuvvetinde %57'lik bir artış gözlemlendi. Ayrıca artan gerinim hızı ile deformasyon modunda bir değişiklik tespit edildi. Dinamik yükleme aralığında civata torkundaki artış, deformasyon modunda bir değişikliğe ve nihai kırılma kuvvetinde %5'lik bir artışa sebep oldu.

TABLE OF CONTENTS

LIST OF FIGURES	vii
LIST OF TABLES	xv
CHAPTER 1. INTRODUCTION	1
CHAPTER 2. LITERATURE REVIEW	2
2.1. General Effects on Composite Bolted Joints.....	2
2.2. Modelling of Composite Bolted Joints	4
2.3. Dynamic Testing of Composite Bolted Joints.....	9
2.4. Motivation of Study	16
CHAPTER 3. EXPERIMENTAL STUDY	18
3.1. Scope of ASTM D5961 Standard	18
3.2. Sample Preparation	20
3.3. Hole Drilling	23
3.4. Quasi-static Tension Bearing Test	25
3.5. Tension Split Hopkinson Pressure Bar Bearing Test.....	26
CHAPTER 4. NUMERICAL STUDY	31
4.1. MAT_162 Material Model	31
4.2. Modelling Methodology.....	35
CHAPTER 5. RESULTS AND DISCUSSION.....	39
5.1. Quasi-static Bearing Test Results	39
5.2. Dynamic Bearing Test Results	44
5.3. Numerical Results	50

CHAPTER 6. CONCLUSION	59
APPENDIX A. BEARING TEST FAILURE CODES WITH ILLUSTRATIONS OF COMMON MODES	61
REFERENCES	62

LIST OF FIGURES

<u>Figure</u>	<u>Page</u>
Figure 2.1. Load-displacement curves of the composite bolted joints at (a) different tightening torques and (b) washer sizes	3
Figure 2.2. Microscope image of countersunk bolt hole bearing damage	4
Figure 2.3. Load-displacement curves of (a) adhesive bonded (b) bolted (c) hybrid bonded composite joints	4
Figure 2.4. Comparison of in plane bearing stress in ref.....	5
Figure 2.5. Load-displacement comparison between simulation and experiment in ref.	6
Figure 2.6. Load carrying capacity of bolted joints at different preloads	7
Figure 2.7. Comparison of explicit and implicit method and experimental results	7
Figure 2.8. Load-displacement curve comparison of tests and numerical models (friction coefficients given in order: bolt-laminate, washer-laminate and laminate-laminate)	8
Figure 2.9. Force-displacement curves of two bolt single lap test configuration (a) displacement data acquired from cross-head (b) displacement data acquired with DIC (digital image correlation) method.....	9
Figure 2.10. Load-displacement curves of different loading velocities	10
Figure 2.11. Load-displacement curves of single lap bearing tests at different loading velocities	11
Figure 2.12. Schematic of a bearing mode energy absorption test and typical force displacement result	11

<u>Figure</u>	<u>Page</u>
Figure 2.13. Comparison of quasi-static and dynamic test results (a) with pin connection (b) with single-lap bolt connection (c) with double-lap bolt connection	12
Figure 2.14. Bearing stress versus bearing strain curve of single bolt quasi-static and dynamic tests at cross-head speed of (a) 5 m s ⁻¹ (b) 10 m s ⁻¹	13
Figure 2.15. (a) the schematic of the TSHPB and (b) the schematic of the dynamic test specimen	14
Figure 2.16. Load displacement curves under quasi-static loading ply orientation of (a) single lay-up (b) complex lay-up	14
Figure 2.17. Load displacement curves under dynamic loading ply orientation of (a) single lay-up (b) complex lay-up	15
Figure 2.18. Failure behavior of bolted joints loaded in tension	16
Figure 2.19. Load transfer curves and correlating failure mode images tested with (a) E/D ratio of 1 (b) E/D ratio of 2 (c) E/D ratio of 3 (d) E/D ratio of 4	16
Figure 3.1. Schematic illustration of (a) single-shear (b) double-shear.....	19
Figure 3.2. Schematic illustration of deformation modes (a) tension (b) shear (c) cleavage (d) bearing (e) fastener pull-through (f) fastener failure	19
Figure 3.3. Technical drawing of the C Procedure fixture	20
Figure 3.4. Microscope images of sample (a) perpendicular to 0° (b) perpendicular to 90°	21
Figure 3.5. Technical drawing of the (a) quasi-static test specimen (b) dynamic test specimen	21
Figure 3.6. Photo of the quasi-static specimen	22
Figure 3.7. Photo of the composite cutting machine	22
Figure 3.8. Figure 3.8. Cutting surface and back surface pictures of drilled holes with (a) water jet (b) milling machine with pointy tip (c) milling machine with bump tip (d) CNC milling machine with bump drill bit	24

<u>Figure</u>	<u>Page</u>
Figure 3.9. Quasi-static bearing test set-up	26
Figure 3.10. Schematic illustration of TSHPB	27
Figure 3.11. Picture of oscilloscope and amplifier	28
Figure 3.12. Picture of dynamic tests specimen fixed to apparatuses	28
Figure 3.13. Technical drawing of TSHPB incident bar fixture apparatus	29
Figure 3.14. Technical drawing of TSHPB transmitter bar clamp apparatus.....	29
Figure 3.15. TSHPB bearing test set up	29
Figure 4.1. Quasi-static model specimen (a) top view (b) side view.....	36
Figure 4.2. Quasi-static model isometric view of (a) apparatus (b) bolt	36
Figure 4.3. Quasi-static model (a) top view (b) isometric view (c) side view.....	37
Figure 4.4. Dynamic model (a) top view (b) isometric view (c) side view	38
Figure 5.1. The force-displacement curves of quasi-static bearing tests at 3.33×10^{-5} $m s^{-1}$ and under a bolt torque of 2.5 Nm	41
Figure 5.2. Figure 5.2 The deformation pictures of composite specimen at (a) 38th (b) 39th (c) 55th (d) 60th second of the quasi-static test, cross-head velocity of $3.33 \times 10^{-5} m s^{-1}$ and bolt torque of 2.5 Nm	41
Figure 5.3. The division of force-displacement curves	42
Figure 5.4. The force-displacement curves of quasi-static bearing tests at a loading velocity of $3.33 \times 10^{-5} m s^{-1}$ and under a bolt torque of 10 Nm	42
Figure 5.5. Quasi-static force-displacement curves with 2.5 Nm bolt torque and 1.66 $\times 10^{-3} m s^{-1}$ cross-head velocity	43
Figure 5.6. Deformation pictures of composite specimen at (a) 0.5th (b) 0.79th (c) 0.93th (d) 1.15th second of the quasi-static test, cross-head velocity of $1.66 \times 10^{-3} m s^{-1}$	44

<u>Figure</u>	<u>Page</u>
Figure 5.7. Incident, reflected and transmitter voltage readings of the tests at (a) 2.5 and (b) 10 Nm bolt torque.....	46
Figure 5.8. Force-displacement curves at 12.68 m s ⁻¹ and 3.33 x10 ⁻⁵ m s ⁻¹ at (a) 2.5 and (b) 10 Nm bolt torque	47
Figure 5.9. Deformation pictures of composite specimen after (a) 0.000033 (b) 0.000067 (c) 0.0001 second the dynamic test started, with loading velocity of 12.68 m s ⁻¹ and 2.5 Nm bolt torque	48
Figure 5.10. Deformation pictures of composite specimen after (a) 0.000033 (b) 0.000067 (c) 0.0001 second after the dynamic test started, with loading velocity of 12.68 m s ⁻¹ and 10 Nm bolt torque	49
Figure 5.11. Comparison of quasi-static models with various EEXPN values	51
Figure 5.12. Deformation pictures of model history variable#10 (a) crack initiation (b) side cracks (c) perpendicular stress wave through fiber direction	51
Figure 5.13. Numerical deformation pictures of the quasi-static model and corresponding test specimen	52
Figure 5.14. Von Mises deformation pictures of the quasi-static model (a) crack initiation (b) side cracks and perpendicular stress wave through fiber direction	53
Figure 5.15. Von Mises deformation pictures of the velocity implemented dynamic model (a) crack initiation (b) perpendicular stress wave through fiber direction	53
Figure 5.16. Comparison of dynamic models with various EEXPN values	54
Figure 5.17. Comparison of dynamic reference test and velocity implemented numerical model	54
Figure 5.18. Comparison of pulse implemented dynamic model and the reference dynamic test	55

<u>Figure</u>	<u>Page</u>
Figure 5.19. Deformation pictures of velocity implemented model (a) before crack initiation (b) first crack (c) shear out deformation mode (d) third crack ..	56
Figure 5.20. Deformation pictures of the pulse implemented dynamic model (a) before crack initiation (b) first crack (c) shear out deformation mode (d) third crack	57
Figure 5.21. Deformation pictures of the velocity implemented model history variable#10 (a) shear-out formation (b) second crack stress localization (c) side stress waves (c) perpendicular stress wave through the fiber direction.....	58

LIST OF TABLES

<u>Table</u>	<u>Page</u>
Table 3.1. C Procedure test parameters	19
Table 4.1. Unidirectional Carbon/Epoxy MAT_162 parameters	34
Table 4.2. MAT_162 material parameter explanations.	34

CHAPTER 1

INTRODUCTION

Fiber reinforced polymer composites (FRPC) are preferred over conventional materials for their high strength to weight ratios. A noticeable application of FRPCs is in the aerospace industry in which the performance of a structure or component is more important than its cost. In many engineering structural designs, the composites parts are required a mechanical fastening either to a composite part or to a metal part. The most common way of fastening composite parts is to apply a bolted connection as it is simpler, easier to apply, and more economical and it allows to disassemble the fastener for repairs. The deformation mode of composite bolted joints is crucial as the joints may fail catastrophically without energy absorption. The deformation mode of composite joints is function of many parameters such as the ply orientation, bolt torque, loading velocity and etc.. Due to countless possible variations and complex distribution of load, understanding the failure of composite bolted joints can be a difficult task. The majority of the experimental and numerical studies on the bolted composite joints have been so far performed at quasi-static loading rates. The composite bolted joints may also be subject to dynamic loads such as bird strike or foreign body impact. But, only few studies have covered the dynamic loading rates.

This thesis study was aimed to investigate the effect of loading rates on the composite bolted joints. For that, a unidirectional carbon fiber reinforced epoxy composite (66-ply) with a bolted joint was tested at the velocities of $3.33 \times 10^{-5} \text{ m s}^{-1}$ and $1.66 \times 10^{-3} \text{ m s}^{-1}$. While the dynamic tests were performed in a Tension Split Hopkinson Pressure Bar (TSHPB) using specially designed specimen grips at 12.68 m s^{-1} . The effect of bolt torques were also investigated at the quasi-static and dynamic velocities. The tests were modelled in the LSDYNA by using MAT_162 composite material model which took in to account the strain rate effects.

CHAPTER 2

LITERATURE REVIEW

The literature survey given below consists of three parts. The most important parameters effective on the bearing strength of the composite bolted joints, the bolt type, applied torque, edge distance to hole diameter ratio (E/D), plate width to hole diameter ratio (W/D) and ply orientation, are summarized. In the second part, a summary of the previous quasi-static and dynamic numerical studies is provided. The results of previous high strain rate tests on the composite bolted joints are given in the last part.

2.1. General Effects on Composite Bolted Joints

Khashaba et al.¹ studied experimentally the effect of tightening torque and washer size on the bearing force of the composite bolted joints ($[0/\pm 45/90]_s$ glass fiber reinforced epoxy composites laminates) using a double-lap test set-up. The studied tightening torques of 0, 5 and 15 N m and the outer diameter of washers ranged 14-27 mm. Bearing force was shown to increase with increasing tightening torque (Figure 2.1(a)), which was ascribed to the increased load carrying area of the bolt at increasing pressures. Increasing washer size (D_w) from 18 to 27 mm led to an increase in the displacement values, but it decreased the bearing force (Figure 2.1(b)). The maximum bearing strength was found in the bolted joint specimens with 18 mm washer size and 15 Nm tightening torque. This combination was reported to form an optimum contact pressure and lateral constrained area. The failure of the composite test samples were reported to occur sequentially with the start of delamination between 0° , $\pm 45^\circ$, and 90° layers due to different strain levels of plies and then proceeded with the net tension of the 90° layers and shear-out failure of the 0° layers. The composite samples failed catastrophically once the bearing failure of $\pm 45^\circ$ layers occurred.

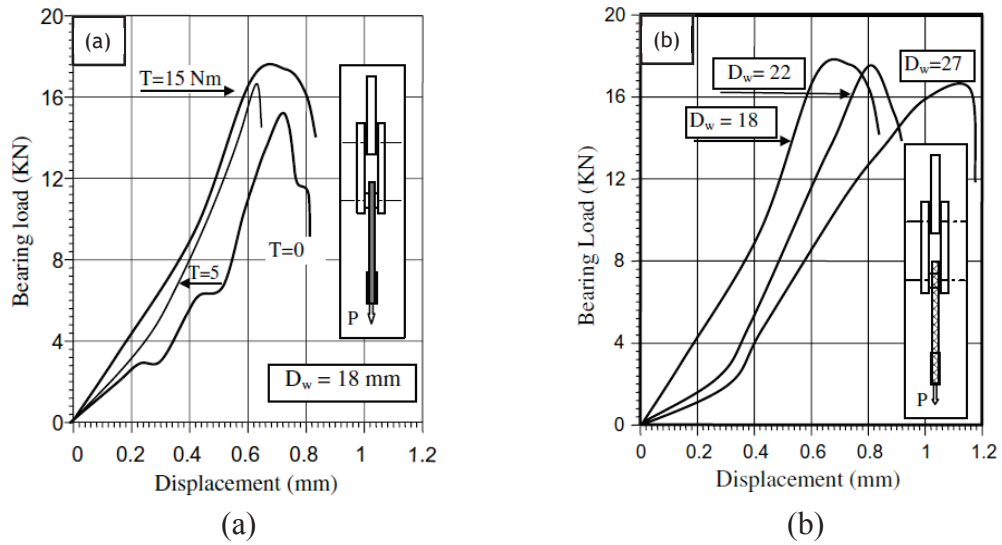


Figure 2.1. Load-displacement curves of the composite bolted joints at (a) different tightening torques and (b) washer sizes ¹

Sen et al. ² studied the effects of E/D, W/D and pre-loads on the bearing strength of glass fiber reinforced laminated plates with three different stacking sequences; $[0^\circ/0^\circ/45^\circ/\pm 45^\circ]_s$, $[0^\circ/0^\circ/45^\circ/45^\circ]_s$ and $[0^\circ/0^\circ/30^\circ/30^\circ]_s$. The results showed that when the W/D or E/D and bolt pre-load increased, the bearing strength of the composites increased nearly for all configurations. At E/D=1, the composite joints failed by cleavage, shear out or net tension (See Appendix A for the bearing test failure codes with illustrations of common modes of Polymer Matrix Composite Laminates). At E/D ratios greater than 2, the plates failed by bearing mode, which was the best mode resisting tensile load. The stacking sequence was shown much effective on the failure modes and bearing strengths of the composite laminated plates and the highest bearing strength was found in $[0^\circ/0^\circ/45^\circ/45^\circ]_s$ plates.

Nezhad et al. ³ studied the damage progression in a carbon fiber-reinforced polymer composite bounded with countersunk bolts. The microscope analysis of internal damage formation showed that the dominant failure was fiber cluster breakage at the countersunk head to specimen contact area as shown in Figure 2.2. The buckling of the 0° fibers was also seen along the delamination between plies.

Kweon et al. ⁴ studied the effects of three different types of joining techniques on the bearing strength of composite-to-aluminum double lap joints. The study showed that hybrid joining was only effective when the mechanical fastening was stronger than adhesive bonding (Figure 2.3(a-c)).

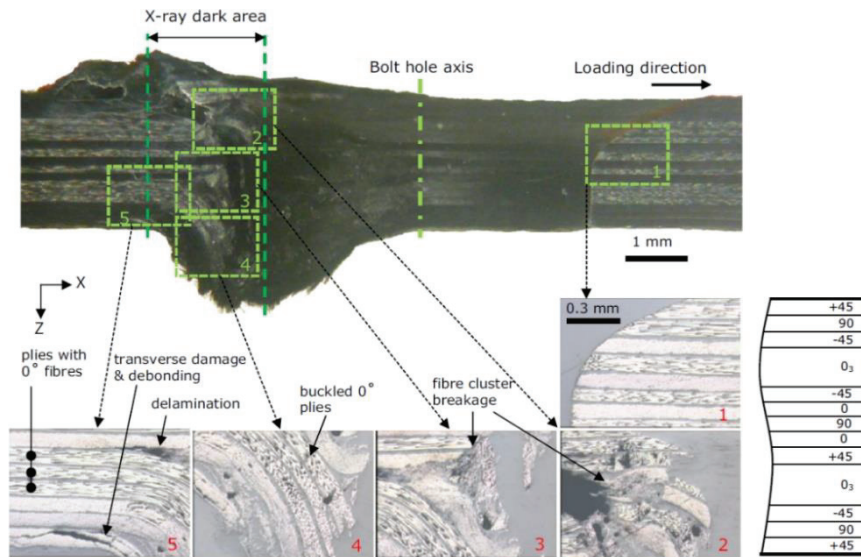


Figure 2.2. Microscope image of countersunk bolt hole bearing damage ³

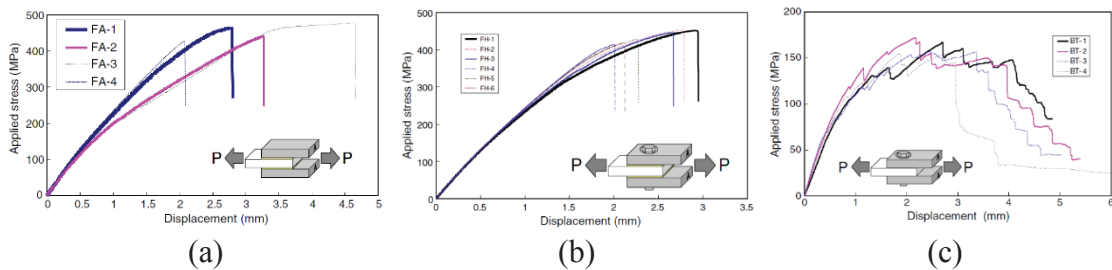


Figure 2.3. Load-displacement curves of (a) adhesive bonded (b) bolted and (c) hybrid bonded composite joints ⁴

2.2. Modeling of Composite Bolted Joints

Gomez et al. ⁵ used MAT_162, a progressive damage model in the LS-DYNA, to investigate the effects of strain rate on the pin and bolt fastened connections at different loading rates. In this work, each lamina of $[0^\circ/90^\circ/\pm 45^\circ]_s$ laminate was modeled separately and the contacts defined by using the fracture toughness data. The simulations underestimated the load and strain values of the tests, while the initial peak loads of the numerical model and the tests were correlated well with each other but force levels of the numerical model showed greater oscillatory behavior. This was due to the instantaneous energy degradation of eroding elements, while in the tests the debris was the source of

sustained load data. It was concluded that the load experienced by the joints at dynamic tests was required to be measured by strain gage.

Tserpes et al. ⁶ developed a 3D progressive damage model using the Hashin failure criteria ⁷ and the degradation rules were taken from Shokrieh et al. ⁸. The study aimed to predict the deformation modes including out-of-plane stress components which were usually neglected. Results showed that the model well agreed with the Nuismer and Whitney's analytical solution ⁹ (Figure 2.4) and the failure modes were successfully predicted. The results also showed that the bolt position significantly affected the strength of joints: a bearing failure was found at high E/D and W/D ratios and shear-out and tension failure were found at low E/D and W/D ratios, respectively.

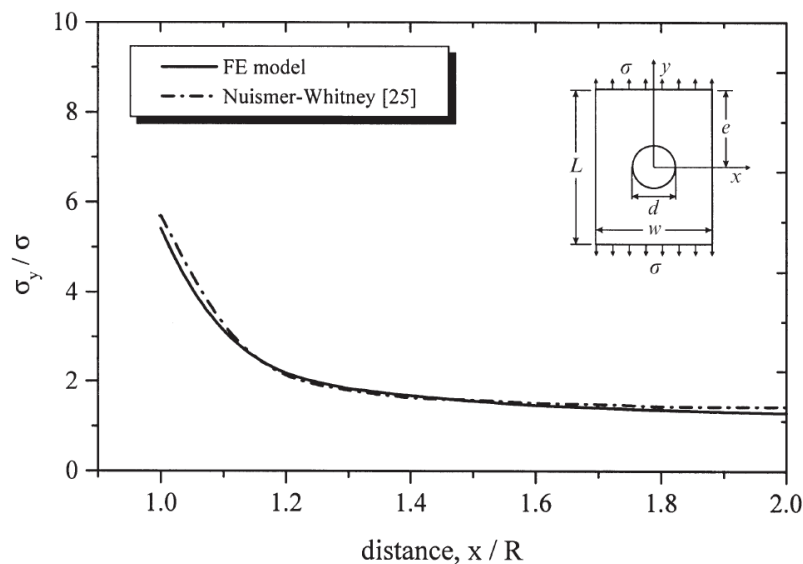


Figure 2.4. Comparison of in plane bearing stress in ref. ⁶

Heimbs et al. ¹⁰ studied the composite fuselage frames (Cytac 977-2/HTS, a unidirectional carbon fibre/epoxy) crash energy absorption in order to create a database for model validations. The numerical models were created in the Abaqus/Explicit FEM program and validated against test data. Validated models were then used to create a fuselage frame crash analysis. Since no strain rate effect was seen until about 10 m s^{-1} in the tests, the rate effects were also neglected in the model. Validated fuselage frame crash simulation showed frame breaking, skin damage under the bending and joint failure as the main crash energy absorption contributors. Pearce et al. ¹¹ validated the static and dynamic pull-through deformation modes of the bolted T300/Cycom970 plain weave fabric ($[(45/0)_4]_s$ layup) composite joints using the stacked-shell modelling approach.

Delamination was shown to play an important role in pull-through failure and altering strain energy release rate resulted in an insignificant change in the load-displacement behavior of joints. Results also showed that stacked-shell approach was an efficient way for predicting the pull-through deformation (Figure 2.5).

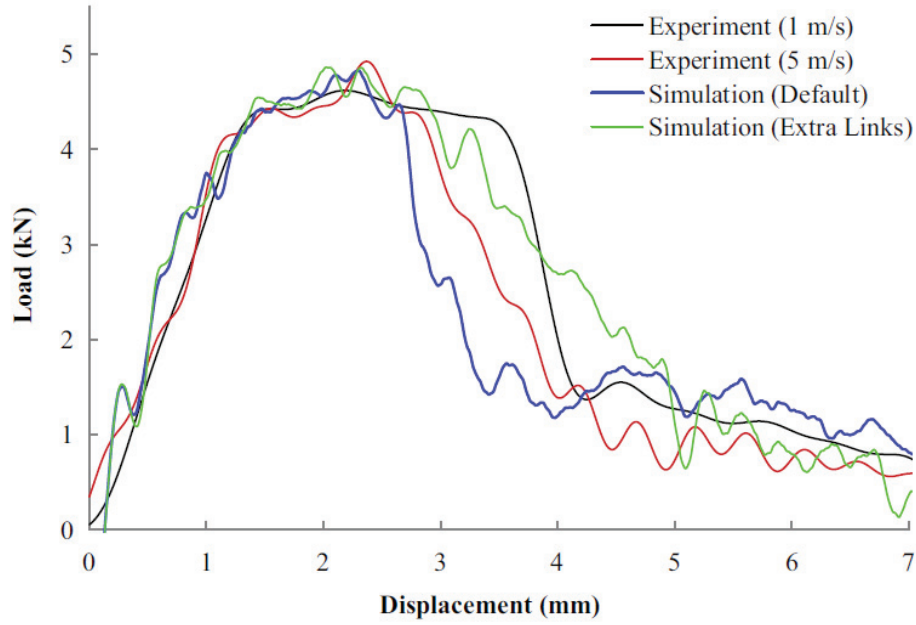


Figure 2.5. Load-displacement comparison between simulation and experiment in ref. ¹¹

Liu et al. ¹² studied experimentally and numerically the effect of bolt-hole fit conditions on the single-lap composite bolted joints under different bolt preloads. The tested composite plate was a hybrid of an unidirectional tape lamina (CYCOM 977-2-35%-12KH7S-134-300) and twill woven carbon fabric composite (CYCOM 977-2A-37%-3KH7A-5HS-280-1200 of Cytec Industries Inc.) with $[(\pm 45)/0/\pm 18/\pm 36/+54/(0/90)/54/\pm 72/90]_s$. The study showed that increasing preload did not always lead to an increasing maximum load and the combination of clearance and preload had to be optimized in order to reach the maximum load carrying capacity. With fixed clearance, increasing preload led to higher maximum load capacities because of enlarged load effective area; however, after some point, the maximum load decreased due to the premature damage formation on the matrix and the fiber (Figure 2.6).

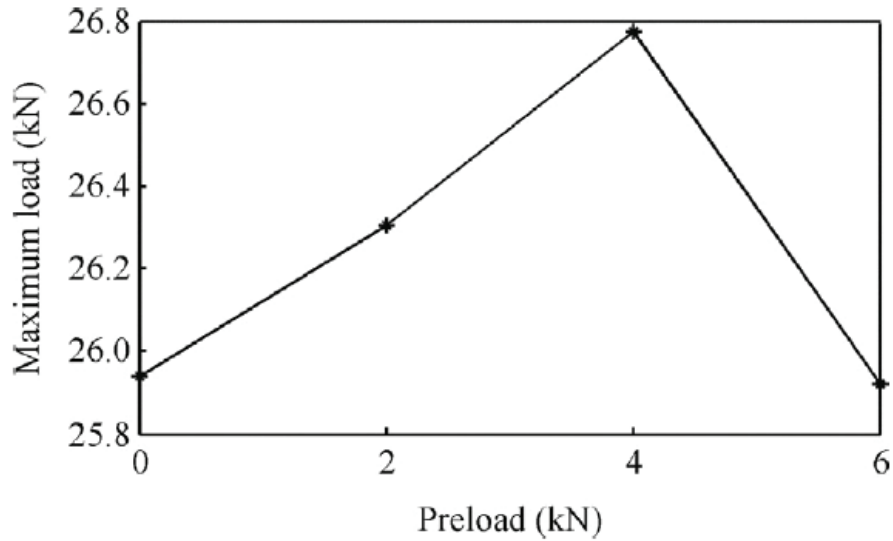


Figure 2.6. Load carrying capacity of bolted joints at different preloads ¹²

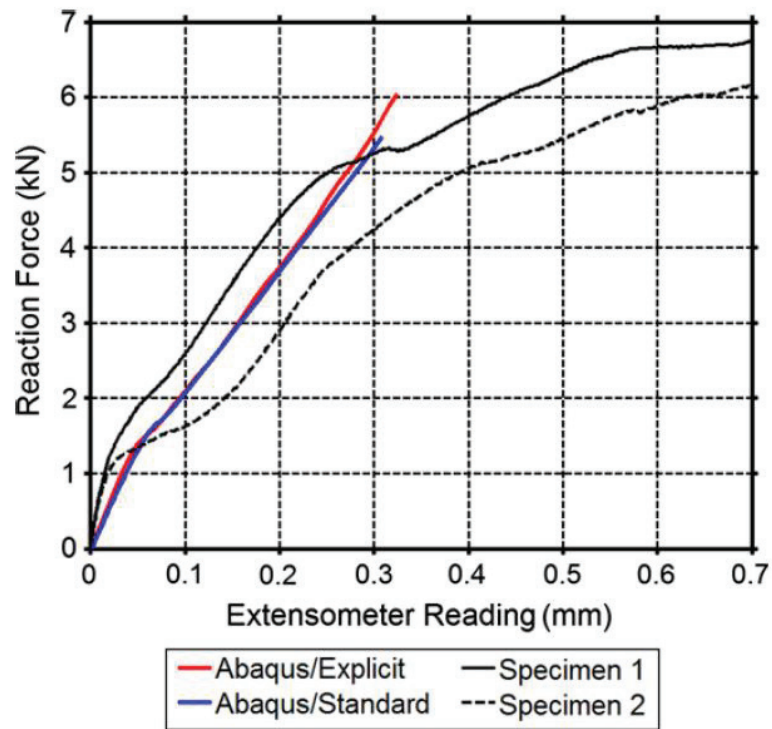


Figure 2.7. Comparison of explicit and implicit method and experimental results ¹³

Egan et al.¹³ studied the behavior of single-lap countersunk bolt fastened carbon–epoxy composite with 17-ply layup with the [+45/90/-45/0/0/0/-45/0/90/0/+45/0/0/0/-45/90/+45] ply sequence both experimentally and numerically. Implicit and explicit methods in Abaqus were compared with each other and verified by the tests results. The

models showed a good match with the experiments and also with each other as shown in Figure 2.7 showing the possibilities of the used of explicit models in the modelling composites joints.

Zhou et al.¹⁴ developed a model using Puck's failure criteria¹⁵ to capture delamination-like, transverse cracking-like or mixed deformation modes and studied the effects of clearance and mesh sensitivity on the composite (carbon fiber epoxy composite HTA/6376) joints. In the explicit simulations of quasi-static loading, deformation modes biased to bearing because the deletion of elements disturbed the local undeleted elements that led to unwanted compressive damage. Also, the Puck's failure criteria was shown to be suitable for modeling mixed deformation modes and solved the unwanted premature compressive damage problem.

McCarthy et al.¹⁶ studied the effect of friction on the composite bolted joints (HTA/6376 carbon-fiber epoxy composite with a stacking sequence of $[45/0/-45/90]_{5S}$) using a commercial code of MSC Marc. The recommended friction coefficients were 0.1, 0.3 and 0.45 sequentially for the bolt-laminate, washer-laminate and laminate-laminate. The results showed a good agreement in the transition and post-transition region but a poorer correlation in the initial stage (Figure 2.8).

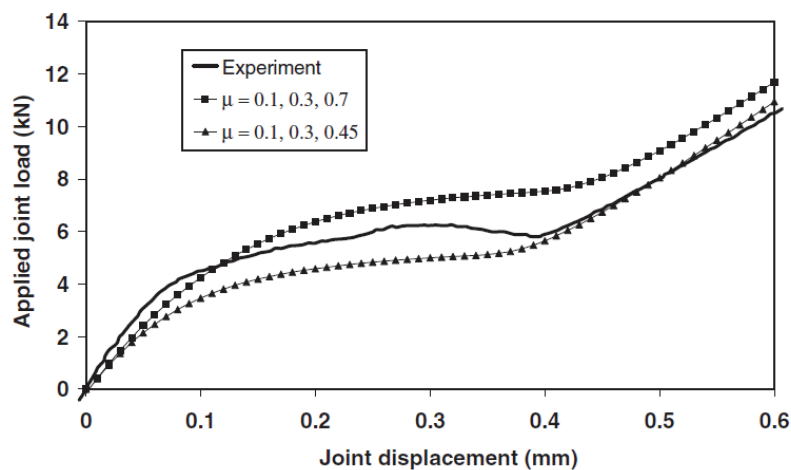


Figure 2.8. Load-displacement curve comparison of tests and numerical models (friction coefficients given in order: bolt-laminate, washer-laminate and laminate-laminate)¹⁶

2.3. Dynamic Testing of Composite Bolted Joints

Heimbs et al. ¹⁷ studied the static and dynamic failure behavior of with 16-ply lay-up carbon fiber composite joints (Cycom 977-2/HTS with a stacking sequence of $[45/90/-45/0]_{2s}$) up to 10 m/s in the single-lap, double-lap shear with variation of one and two countersunk bolts, coach peel and pull-through. The tests showed no velocity effect on the deformation modes and the force-displacement curves. Only the single lap shear test with two bolts showed a different failure mode at increasing velocities, resulting in higher energy absorption (Figure 2.9).

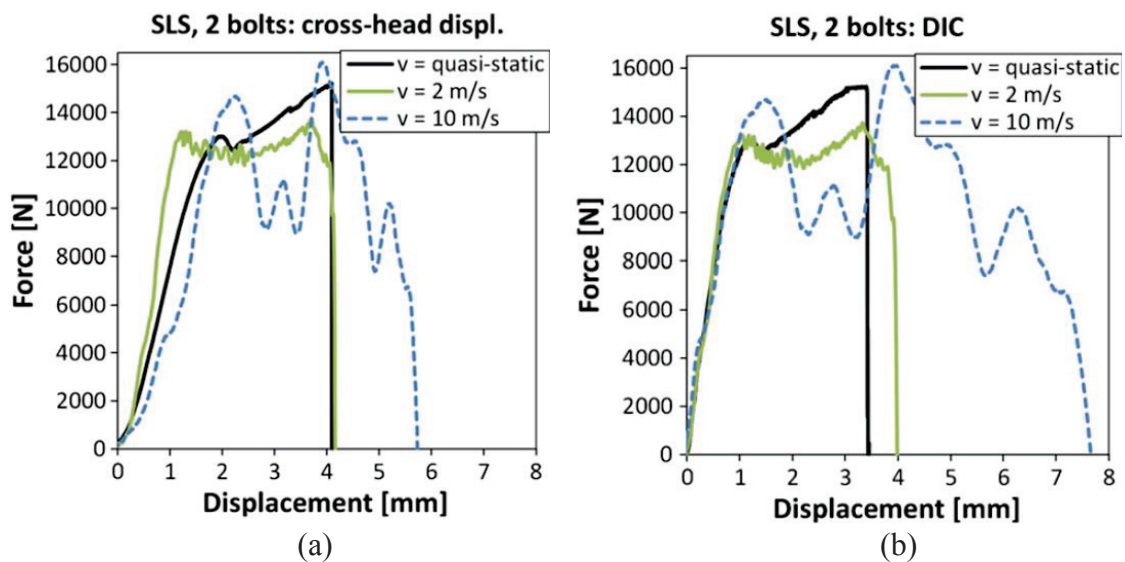


Figure 2.9. Force-displacement curves of two bolt single lap test configuration (a) displacement data acquired from cross-head (b) displacement data acquired with DIC (digital image correlation) method ¹⁷

Portemont et al. ¹⁸ studied the static and dynamic bearing failure of double shear carbon epoxy composites with 16-ply lay-up (Hexcel T700GC with a stacking sequence of $[45/90/-45/0]_{2s}$) with one pin at the loading velocities ranging from 8.3×10^{-3} to 1 m s^{-1} . A specially designed apparatus was used to prevent the unwanted deformation mode of bending. There was a 20% increase in the peak stress with increasing strain rate; however, the stiffness of joint was not influenced by the loading velocity (Figure 2.10).

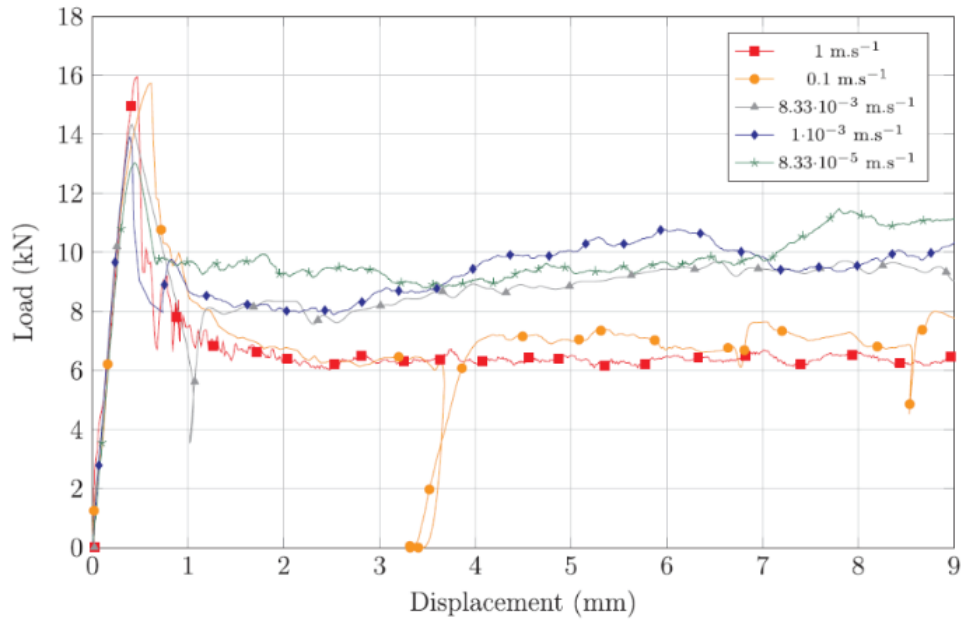


Figure 2.10. Load-displacement curves of different loading velocities ¹⁸

Li et al. ¹⁹ studied the deformation behavior of differently orientated composite bolted joints (CFRP HTA-97(hybrid) $[(\pm 45)F/0U/90U/-45U/45U/90U/0U/(\pm 45)F]$, CFRP HTA-97(fabric) $[(\pm 45)/(0/90)/(\pm 45)/(0/90)/(\pm 45)/(0/90)/(\pm 45)]$, CFRP HTA-97(fabric) $[(\pm 45)/(0/90)/(\pm 45)]$, CFRP HTA-EH25(UD-Tape) $[0/-45/0_2/45/90/-45/0_2/45/90/-45/0_2/45]_s$, CFRP G803-914(fabric) $[(0/90)/(\pm 45)/(0/90)/(\pm 45)/(0/90)/(\pm 45)/(0/90)]$, CFRP HTA-EH25(UD-Tape) $[0_2/-45/90/45/0]_s$) at static and dynamic velocities (4 and 8 m s⁻¹) by means of single and double lap tests. The failure mode changed and the total energy absorption increased as the velocity increased.

Pearce et al. ²⁰ conducted an experimental investigation on the dynamically loaded bolted joints of carbon fiber composites (T300/CYCOM970 plain weave with a stacking sequence of $[45/0]_{4s}$). Single fastener joints were tested both under bearing and pull-through between 0.1 and 10 m s⁻¹. A simple composite structure was tested afterwards to determine whether or not the single fastener rate dependence had any effect on overall response of the bolted composite structure. The rate sensitivity was found to depend on the direction of the applied load for the single lap shear (Figure 2.11). Pull-through specimens did not show any rate dependence but the bearing specimens had increased energy absorption with increasing strain rate and the constructed composite structure showed only a mild rate dependence.

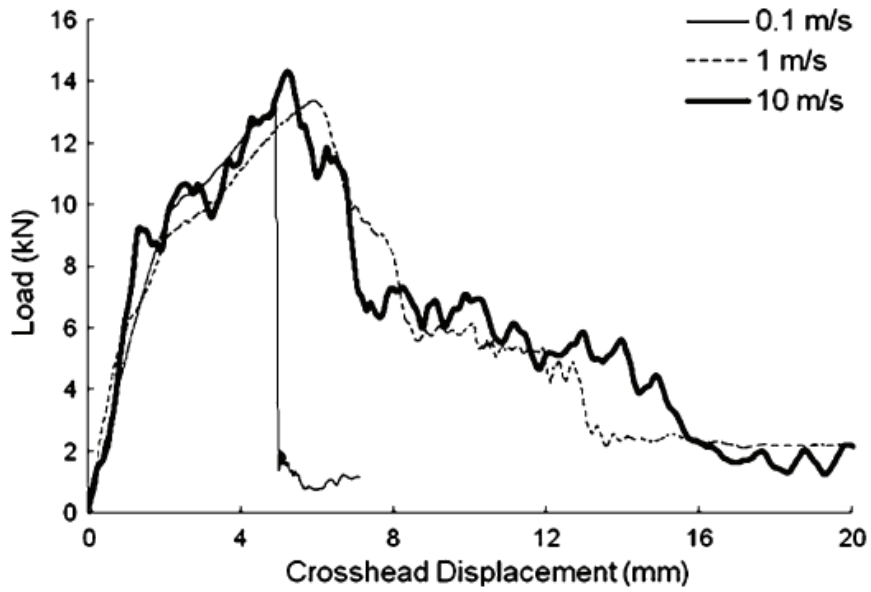


Figure 2.11. Load-displacement curves of single lap bearing tests at different loading velocities ²⁰

Heimbs et al. ²¹ conducted an experimental study to determine the specific energy absorption (SEA) capacity of composites and sandwich plates by pulling bolts at static and dynamic velocities. The schematic of bearing energy absorption test and a typical force-displacement response are shown in Figure 2.12. The effect of different parameters like fiber and matrix material type were also studied. The results showed that increasing pulling velocity reduced SEA significantly. Although the use of ductile fibers had no major advantage, the tougher epoxy resins were superior to brittle ones in terms of energy absorption. The sandwich plates were however shown to have relatively low SEA values.

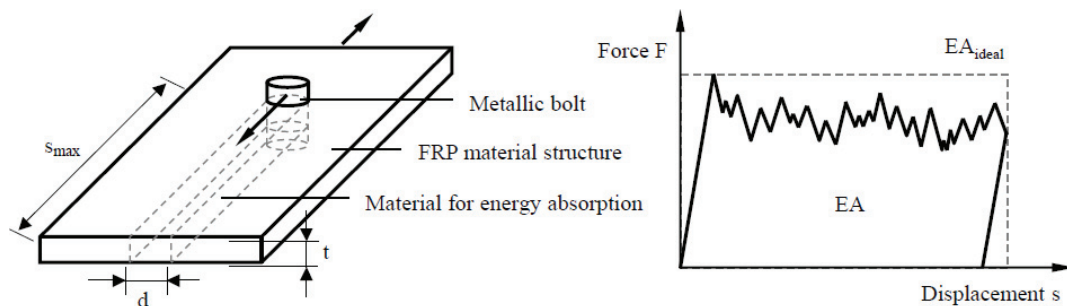


Figure 2.12. Schematic of a bearing mode energy absorption test and typical force displacement result ²¹

Ger et al.²² investigated the effect of pulling velocity on the composite joint (Bestfight ST-2 (Toho Rayon) fiber, Kevlar 49 (DuPont) Kevlar fiber and Ciba-Geigy (Araldite 507 + Hardener 906 + Accelerator DY061) epoxy) configurations. The quasi-static tests were conducted at 0.5 mm/min and the dynamic tests at 3-5 m/s range. The quasi-static and dynamic load-displacement curves of pinned, single-lap and double lap bolted joints are shown in Figures 2.13(a)-2.13(c), respectively. No effect of strain rate was observed on the bearing strengths. The results also showed that pin connection was the weakest in terms of bearing strength.

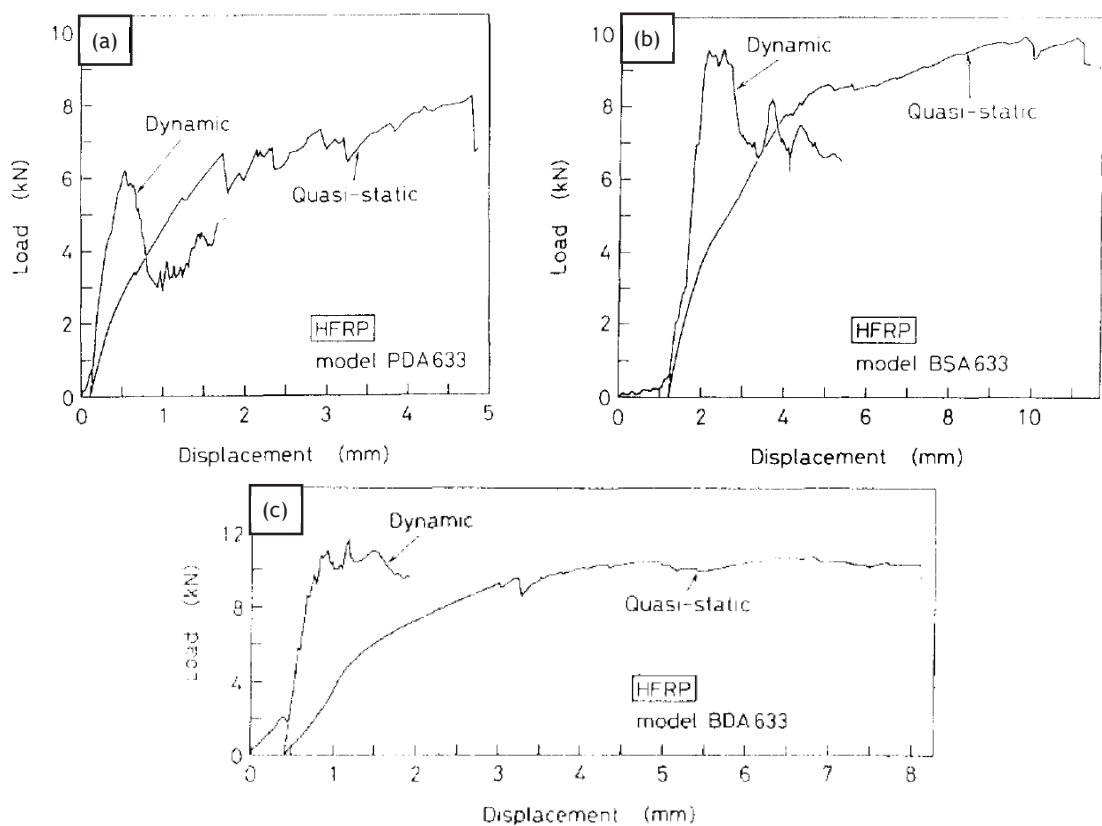


Figure 2.13. Comparison of quasi-static and dynamic test results (a) with pin connection (b) with single-lap bolt connection and (c) with double-lap bolt connection²²

Egan et al.²³ studied single and multi-bolt carbon-epoxy aircraft fuselage joints (HexPly M21E/IMA carbon-epoxy with three different stacking sequence, A-layup [-45/90/45/0/0/45/90/-45/0/0/45/90/-45], C-layup [-45/90/45/0/0/0/45/0/90/0/-45/0/0/0/45/90/-45], E-layup [-45/90/45/0/0/0/-45/45/0/0/0/-45/90/45/0/0/0/-45/45 /0/0/0/-

45/90/45]) at static and dynamic loading rates. The initial failure mode was bearing for all tested specimens, while the final failure was the fastener pull-through or fastener fracture. The quasi-static and dynamic tests results are shown in Figures 2.14(a) and 2.14(b), respectively. The study showed that the thicker specimens had less bearing strength hence less energy absorption, due to fasteners being exposed to much higher loads, leading to fastener fracture or countersunk fastener head breaking.

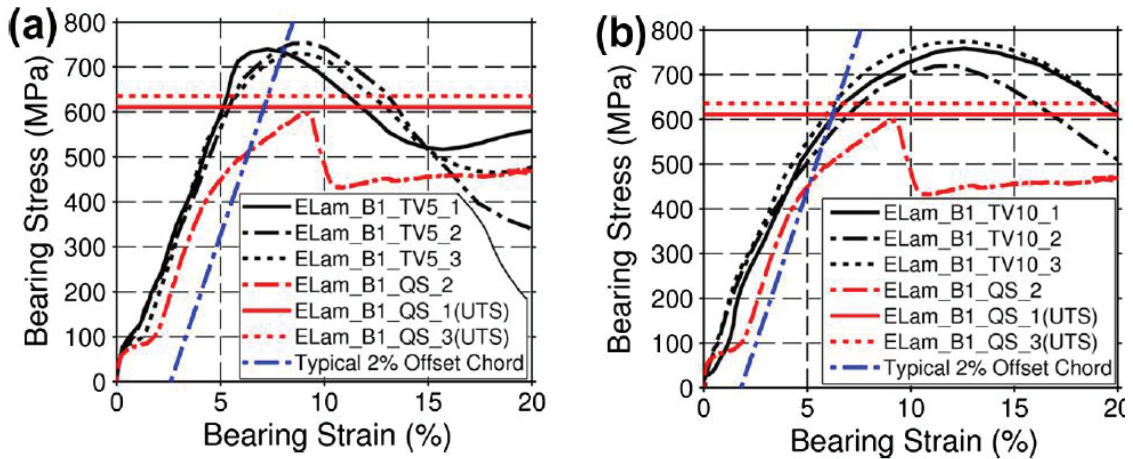
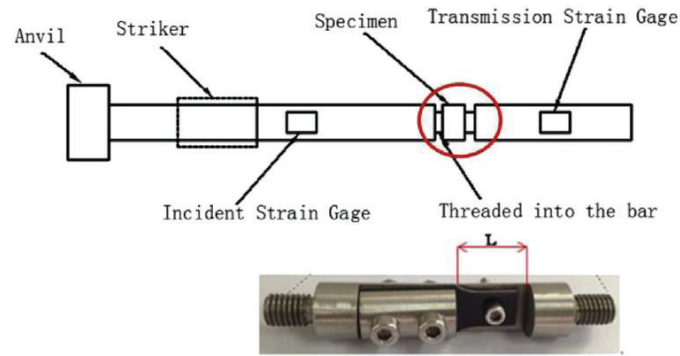


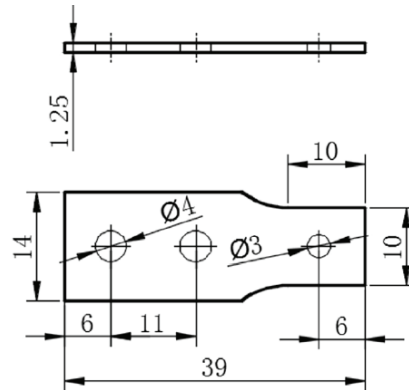
Figure 2.14. Bearing stress versus bearing strain curve of single bolt quasi-static and dynamic tests at cross-head speed of (a) 5 m s^{-1} and (b) 10 m s^{-1} ²³

Wang et al. ²⁴ studied the effect of loading velocity on the ultimate failure load and the stiffness of the composite joints (E-glass fiber reinforced 913 resin matrix) with various stacking sequences ($[0]_{10}$, $[45]_{10}$, $[90]_{10}$, $[90/0/45/0/0]_{10}$, $[90/45/45/0/-45]_{10}$, $[90/45/90/0/90]_{10}$ and $[90/-45/0/45/90/-45/0/45/0/90]_{10}$). A novel advanced and predictive model combining composite laminate theory and Tsai-Hill criterion was used to estimate the strain rate dependency of the stiffness and strength of the bolted joints. Dynamic tests were conducted in the TSHPB with a special designed apparatus shown in Figure 2.15(a). The schematic of dynamic test specimen is also shown in Figure 2.15(b). The used model showed a good compatibility with the experimental results; the errors were only below 12% for the quasi-static tests and 30% for the dynamic tests. Quasi-static test results of single lay-up and complex lay-up and the dynamic tests results of single lay-up and complex lay-up specimens are sequentially shown in Figures 2.16(a) and 2.16(b) and Figure 2.17(a) and 2.17(b). Results showed that the deformation was always parallel to the fiber direction for the single lay-up configuration. The optimal lay-up

configuration was found $[90/0/45/0/0]_{10}$ for both quasi-static and dynamic tests in the terms of stiffness. The largest failure load occurred in the laminates with $[90/-45/0/45/90/-45/0/45/0/90]_{10}$.



(a)



(b)

Figure 2.15. (a) the schematic of the TSHPB and (b) the schematic of the dynamic test specimen²⁴

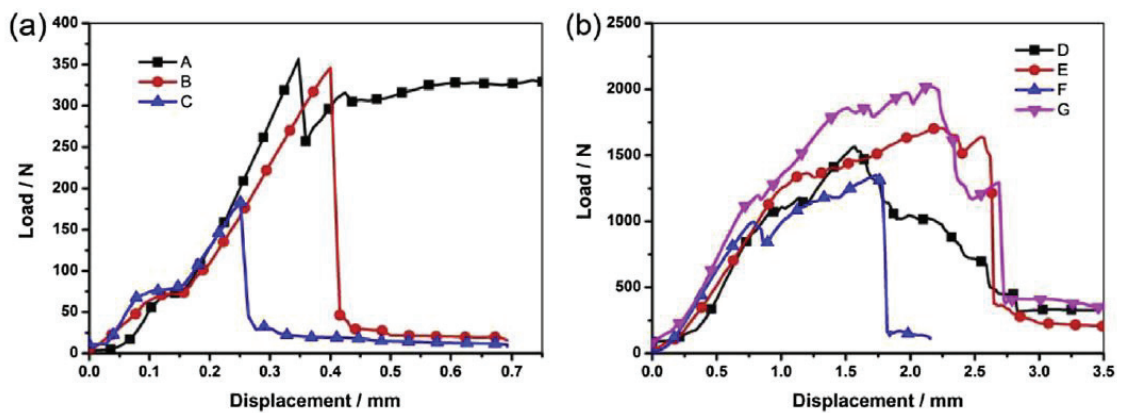


Figure 2.16. Load-displacement curves under quasi-static loading ply orientation of (a) single lay-up and (b) complex lay-up²⁴

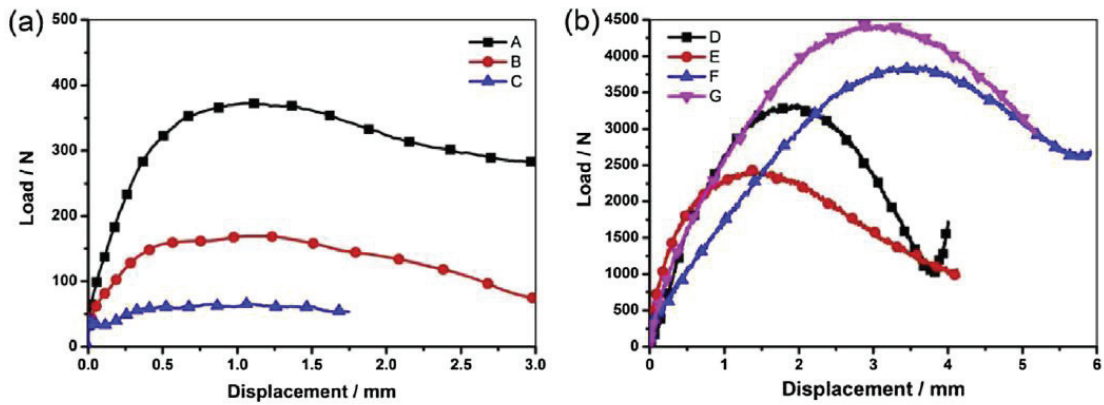


Figure 2.17. Load displacement curves under dynamic loading ply orientation of (a) single lay-up and (b) complex lay-up²⁴

VanderKlok et al.²⁵ studied experimentally the effect of E/D ratio on the deformation mode of composite bolted joints (G-10 FR-4 E-glass ply epoxy resin) at static and dynamic velocities. The high speed tests were conducted in a TSHPB with pulse shaping. The load-displacement curves of dynamic loading are shown in Figure 2.19 for different E/D ratios. The combination of different E/D ratios and loading velocities led to diverse deformation modes. These deformation modes were assigned to different parts of bearing stress versus E/D ratio curve with a deformation mode indication (Figure 2.18).

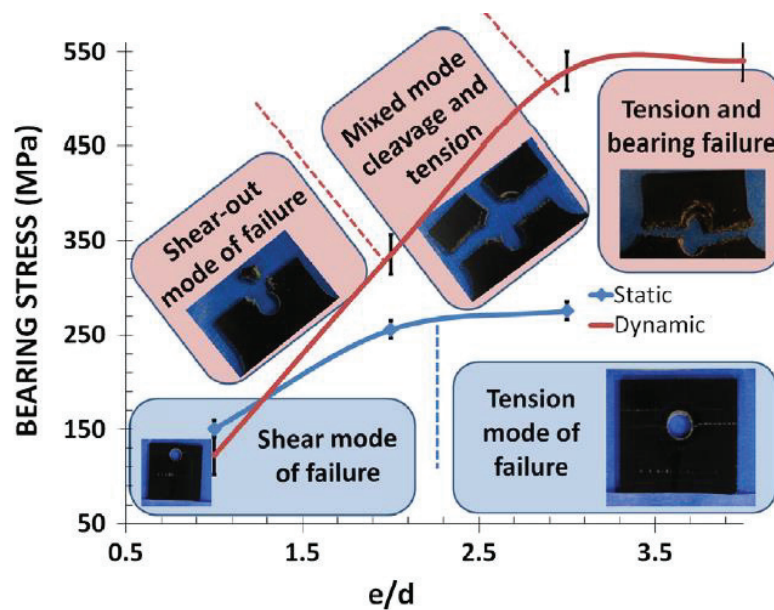


Figure 2.18. Failure behavior of bolted joints loaded in tension²⁵

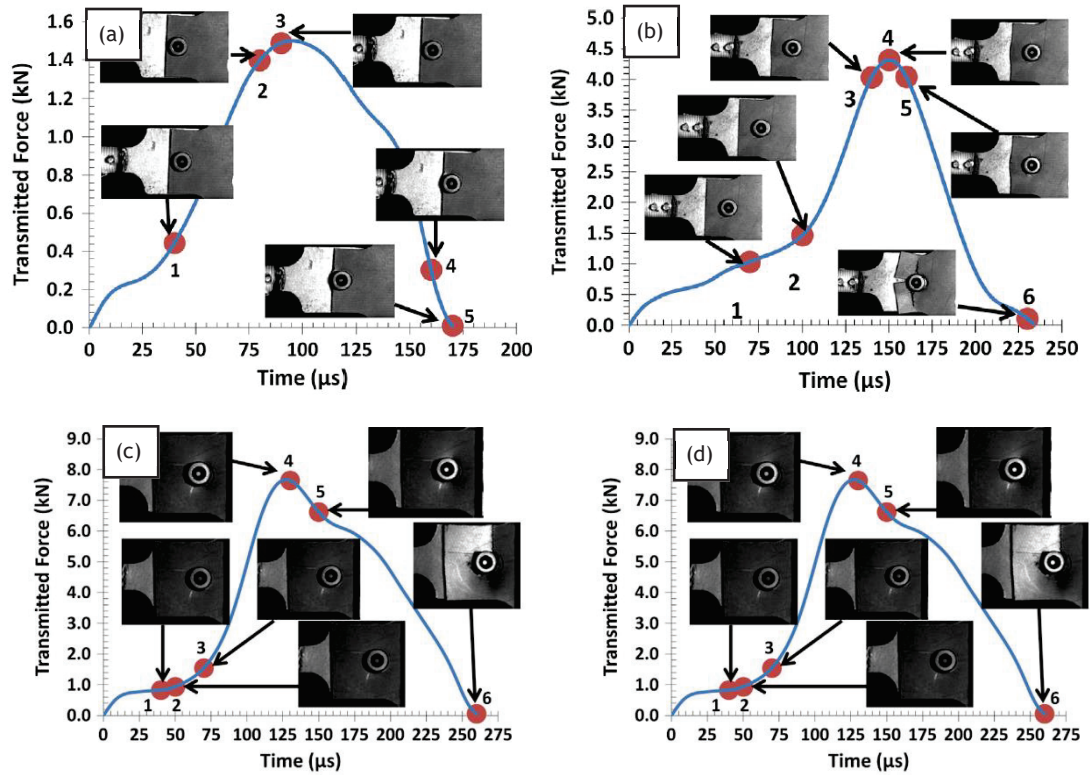


Figure 2.19. Load transfer curves and correlating failure mode images tested with (a) E/D ratio of 1 (b) E/D ratio of 2 (c) E/D ratio of 3 and (d) E/D ratio of 4 ²⁵

2.4. Motivation of Study

Above summary have shown many studies on the composite bolted joints in the literature, many of which were performed at the quasi-static velocities, while there have been only few at high velocities. As shown by Heimbs et al. ¹⁷, the deformation mode of the bolted joints depended on the fiber configuration and altered with changing loading velocity. An increase in the loading rate was commonly found to increase the energy absorption. Few studies reported that the bearing strength also increased with increasing loading rate ^{18, 24, 25}, while others reported no effect of loading rate on the bearing strength of composite bolted joints ^{11, 17, 22}. The raised conflicts may be due to the rate sensitivities of the composites. Although, the studies on the strain rate dependence of the composites showed a low strain rate sensitivity ²⁶, the matrix has a high strain rate sensitivity. For the matrix dominant bearing specimens, bearing strength may increase with increasing

loading rate but fiber dominant bearing specimens may not show any bearing strength increment. There are also numerous variables that can affect the overall strength of composite bolted joints. The increase of clearance increased stiffness ²⁷, and growing washer radius increased the bearing strain ¹. The increase of bolt torque always led to increases in the bearing strength almost regardless of the fiber configuration ^{1, 2}. An increase in the preload restrains the plies and increases the load effective area, resulting higher bearing strengths. Due to the high cost of testing, numerical models are attractive to reduce to the cost of tests and the time of analysis. Despite many numerical studies in the literature, most of them were either 2D or analytical ³ and there were only few real-like numerical studies ⁵. This thesis study was aimed to investigate the effect of loading rates on the composite bolted joints. For that, a unidirectional carbon fiber reinforced epoxy composite (66-ply) with a bolted joint was tested at the velocities of $3.33 \times 10^{-5} \text{ m s}^{-1}$ and $1.66 \times 10^{-3} \text{ m s}^{-1}$. While the dynamic tests were performed in a Tension Split Hopkinson Pressure Bar (TSHPB) using specially designed specimen grips at 12.68 m s^{-1} . The effect of bolt torques were also investigated at the quasi-static and dynamic velocities. The tests were modelled in the LSDYNA by using MAT_162 composite material model which took in to account the strain rate effects.

CHAPTER 3

EXPERIMENTAL STUDY

3.1. Scope of ASTM D5961

The ASTM D5961 covers the bearing response of pinned or fastened joints using multi-directional polymer matrix composite laminates reinforced with high modulus fibers. There are four main test procedures in the ASTM D5961 standard: double-shear tensile loading (Procedure A), single-shear tensile or compressive loading of two-piece specimen (Procedure B), single-shear tensile loading of one-piece specimen (Procedure C) and double-shear compressive loading (Procedure D). The single-shear tensile and double-shear tensile loading tests are shown in Figures 3.1(a) and (b).

The deformations modes are classified in the same standard which include tension, shear, cleavage, bearing, fastener pull-through and fastener failure, shown sequentially in Figures 3.2 (a-f). The procedure C, single-shear tensile loading of one-piece specimen, was selected as a test procedure in the thesis. The ASTM D5961 standard also covers the general specifications of the tests including loading condition, mating material, number of holes, fit clearance, fastener torque, fastener diameter, edge distance ratio. All these specifications are tabulated in Table 3.1. Altering the parameters is allowed if documented. Technical drawing of the Procedure C fixture is given in Figure 3.3.

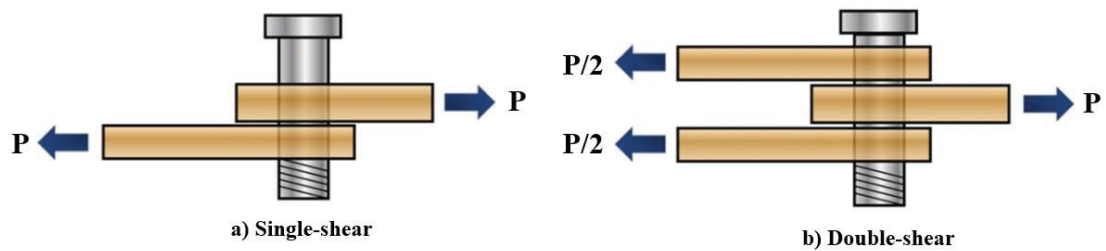


Figure 3.1. Schematic illustration of (a) single-shear (b) double-shear

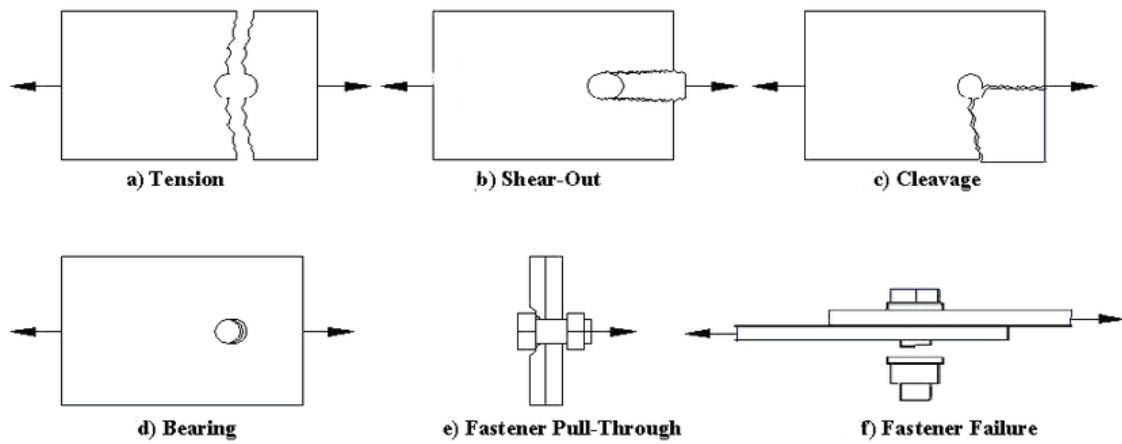


Figure 3.2. Schematic illustration of deformation modes (a) tension (b) shear (c) cleavage (d) bearing (e) fastener pull-through and (f) fastener failure

Table 3.1. Procedure C test parameters

Parameter	Standard
Loading condition	Single shear
Mating material	Steel fixture
Number of holes	One
Fit clearance	Tight
Fastener torque	2,5-3,4 Nm
Fastener diameter	6 mm
Edge distance ratio	3
Width to diameter ratio	6

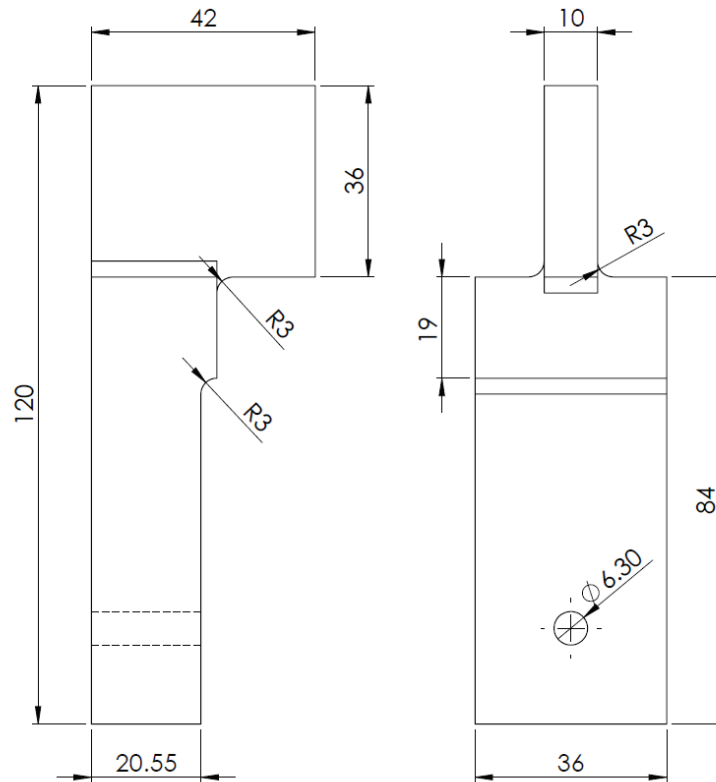
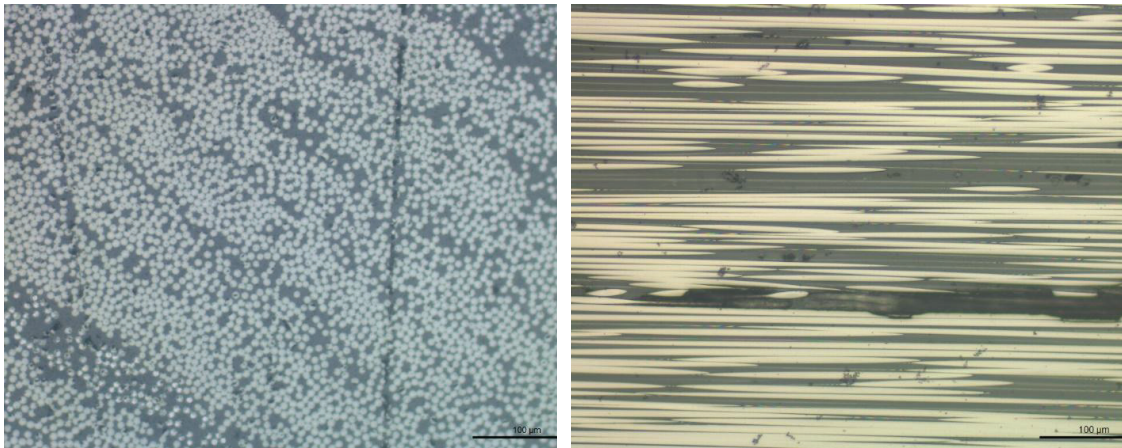


Figure 3.3. Technical drawing of the Procedure C fixture in mm

3.2. Sample Preparation

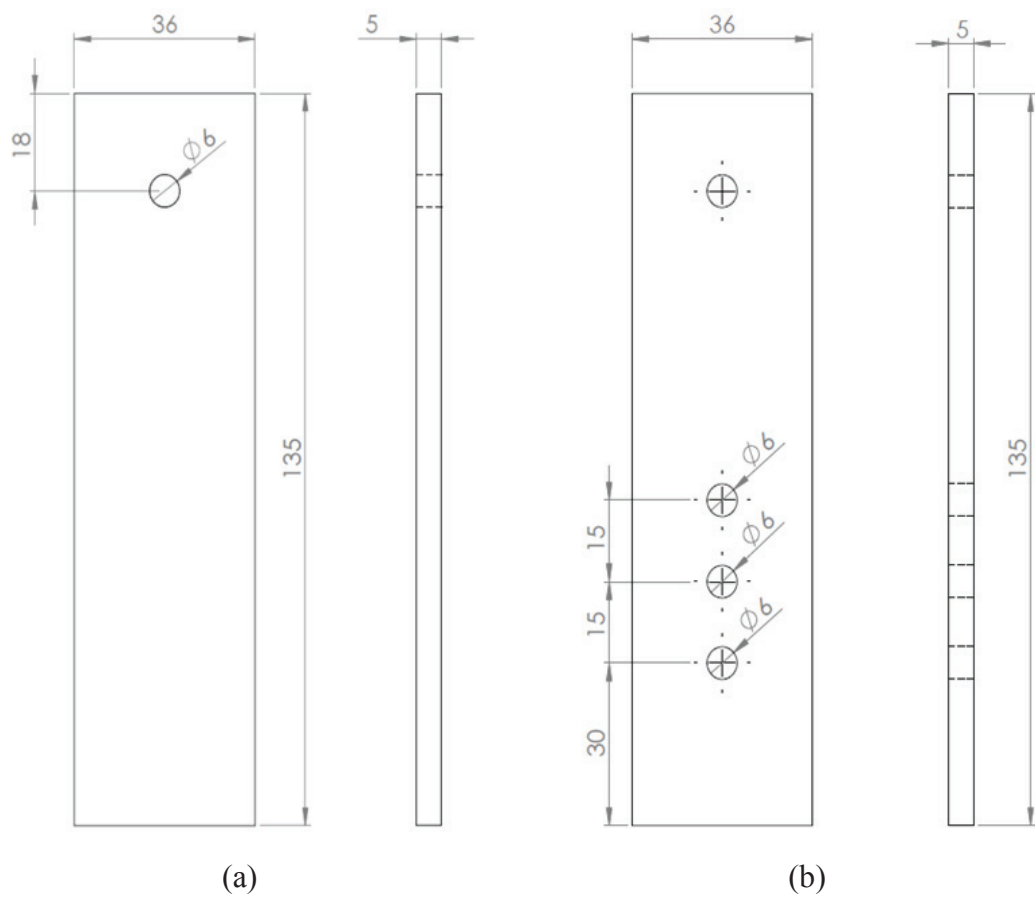
TORAY T300B carbon fiber reinforced/FRD-YG Epoxy laminated composite of single lay-up, [0] degree with 66 plies was selected as specimen. Sample was received as a plate with dimensions of 400x300 mm and a thickness of 5 mm. Received plate was inspected with a microscope (Figure 3.4) for determination of deflections and ply count. Two different sets of specimens were prepared for quasi-static and TSHPB tests. Technical drawings of the specimens were given in Figure 3.5. Samples were cut with a composite cutting machine (Figure 3.7.) to a length of 135 mm and a width of 36 mm, in accordance with ASTM D5961. All specimens have a constant W/D (plate width to hole diameter ratio) ratio of 6 and a E/D (edge distance to hole diameter ratio) ratio of 3. Complete picture of the specimen can be seen on Figure 3.6.



(a)

(b)

Figure 3.4. Microscope images of sample (a) perpendicular to 0° (b) perpendicular to 90°



(a)

(b)

Figure 3.5. Technical drawing of the (a) quasi-static test specimen (b) dynamic test specimen

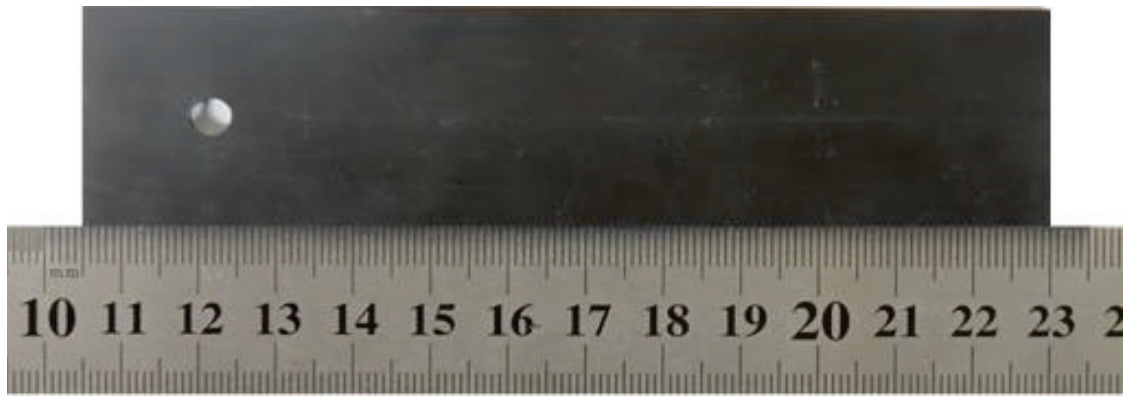


Figure 3.6. Picture of the quasi-static specimen



Figure 3.7. Photo of the composite cutting machine

3.3. Hole Drilling

Drilling a hole compatible with composite is a challenging task due to the anisotropy. Improper drilling methods can cause fiber damage, uneven conical holes and extensive heat can disrupt the structure of the matrix. In order to obtain the composite plates with the minimum possible damage, four different hole drilling methods were investigated before the bearing tests.

The first trial cutting was made using a water jet machine. The water jet machine can cut a wide variety of materials using high pressure water and abrasive mixture. The use of water jet however resulted in a highly conical hole as seen in Figure 3.8(a). The diameter of the hole in Figure 3.8(a) was measured 6 mm on the cut surface and 6.3 mm on the rear surface. But, no matrix or fiber damage was observed on the cut surface, although the rear surface had matrix damage because of the conical cutting nature of the nozzle.

The second trial was made using a milling machine with a pointy end drilling tip of 6 mm. The hole was drilled at 3000 RPM and a coolant was used to prevent excessive heating. The pointy tip caused extensive damage both on the matrix and the fiber as seen in Figure 3.8(b). Most damage was formed when the driller tip was going out, pulling and snatching the fibers. Despite the use of a coolant, the matrix was overheated. The same method with a bump drill bit with 6 mm radius resulted in better hole surfaces. There was no heating of the composite plate and no damage was observed on the matrix. But, when the driller pierced the rear surface of the specimen, the drill snatched the fibers and pulled the fibers out of the matrix as seen in Figure 3.8(c).

The last trial was made using a CNC milling device. The bump drill bit with a 4 mm radius was used. The rotation speed, with or without backing support, feed rate, with or without coolant were altered during milling to obtain a hole with a minimum possible damage. The optimal hole was obtained with a 5000 RPM, a backing wood support, a feed rate of 0.1 mm and a water coolant. There was no matrix damage but minor fiber damage was seen on the rear of the specimen as seen in Figure 3.8(d). The hole drilling was continued with the CNC milling machine using the parameters listed above.

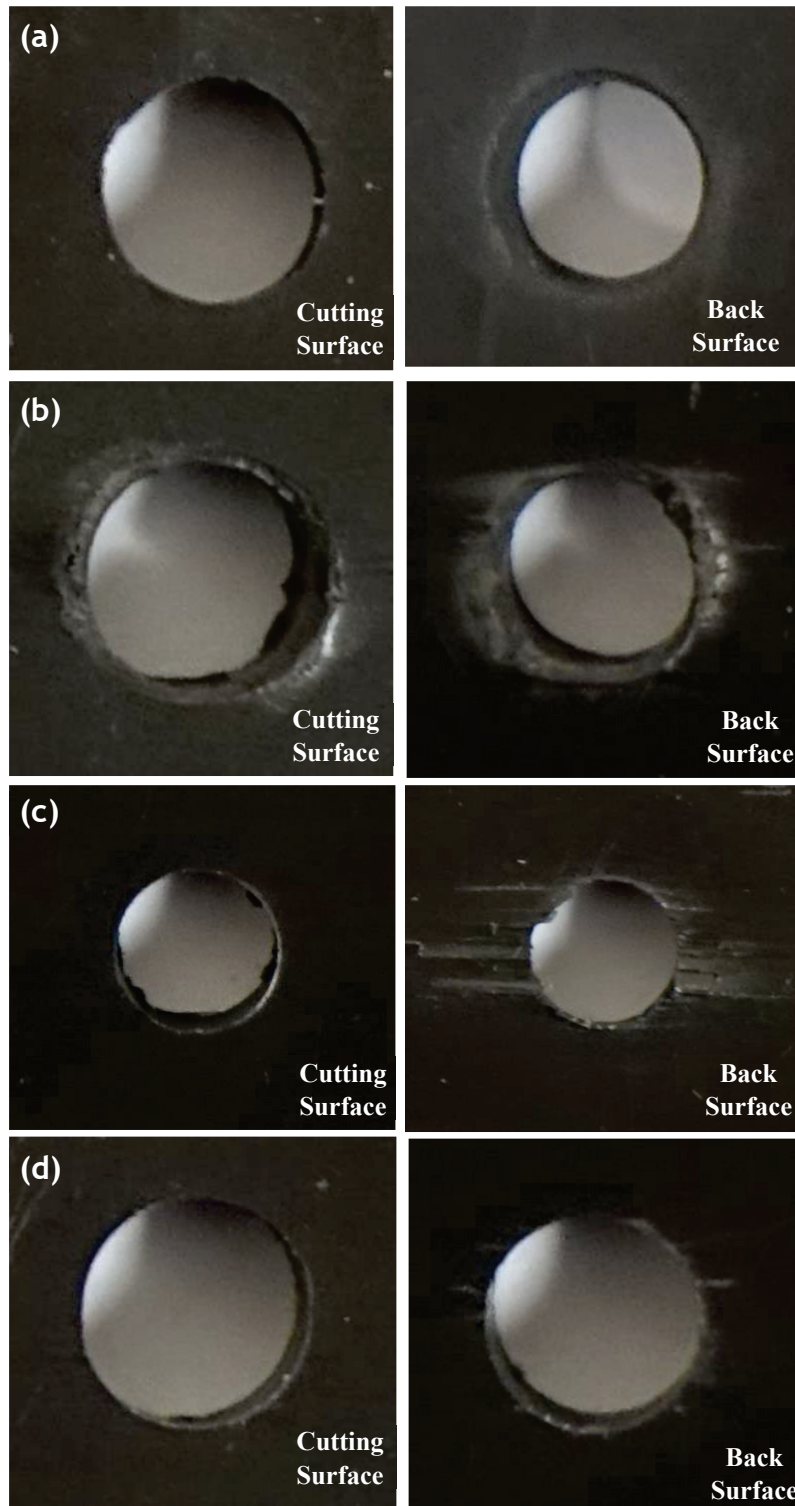


Figure 3.8. Cutting surface and back surface pictures of drilled holes with (a) water jet (b) milling machine with pointy tip (c) milling machine with bump tip (d) CNC milling machine with bump drill bit

3.4. Quasi-Static Tension Bearing Tests

Quasi-static tension tests were performed according to the ASTM D5961 “Bearing Response of Polymer Matrix Composite Laminates” using Shimadzu AG-X Universal Test Machine (Figure 3.9). Tests were performed at two different cross-head velocities, 3.3×10^{-5} and $1.66 \times 10^{-3} \text{ m s}^{-1}$. In the quasi-static tests, the bearing stress is (σ^{br}) determined by using the following equation,

$$\sigma^{br} = \frac{P}{(k \times D \times h)} \quad (3.1)$$

where, P is the load, k is load per hole factor (1 for single-fastener or pin tests and 2 for double-fastener tests), D is the diameter of hole and h is thickness of the specimen. The bearing strain (ε^{br}) was calculated using the following relation,

$$\varepsilon^{br} = \frac{\delta}{k \times D} \quad (3.2)$$

where δ is extensometer displacement. The displacement in the tests was measured using a video extensometer and also calculated from the crosshead speed. The test fixture (technical drawing is given in Figure 3.3.) was made of ST52 steel with a hardness of 42 HV. The fastener was a 8.8 grade stainless steel hex-bolt with a 6 mm diameter. The bolt had a tensile failure load of 16 kN and a shear failure load of 22 kN. The clearance was neat-fit without washers. At $3.3 \times 10^{-5} \text{ m s}^{-1}$ cross-head speed tests, 2.5 Nm and 10 Nm and at $1.66 \times 10^{-3} \text{ m s}^{-1}$ cross-head speed tests 2.5 Nm bolt torques were applied using a torque meter. A P60D sandpaper was used between the sample and the jig to prevent slipping of sample. All tests were recorded by a video camera in order to capture the deformation mode precisely. A total of three tests were performed for each configuration.



Figure 3.9. Quasi-static bearing test set-up

3.5. Tension Split Hopkinson Pressure Bar Bearing Tests

The TSHPB set-up is a widely used method of determining the high strain rate deformation behavior of materials. The principles of the TSHPB are based on uniaxial wave propagation in long bars. The schematic of TSHPB testing is shown in Figure 3.10. The set-up consists of two bars and a tube: incident and transmitter bars and striker tube. The striker tube is fired by the help of a gas gun. Upon the striker tube impacts to the flange at the end of the incident bar a rectangular elastic tension wave is created on the incident bar at the impact side. Then, the tension wave propagates along the bar, when it comes across with the specimen, part of the wave is reflected as a compression wave into the incident bar and rest is transmitted to the transmitter bar as a tensile wave. The relative amounts of the reflected and transmitted stress waves are a function of the mechanical impedance difference between the bars and the sample tested. The incident and transmitted stress waves are measured by the strain gauges mounted on both incident and transmitter bar. The stress (σ_i) and the strain (ϵ_i) created on the incident bar are

$$\sigma_i = \frac{1}{2} \rho_b C_b v_{sb} \quad (3.3)$$

and

$$\varepsilon_i = \frac{1}{2} \frac{v_{sb}}{C_b} \quad (3.4)$$

where, ρ_b , C_b and v_{sb} are the density, elastic wave velocity of the bar and the striker bar velocity, respectively.

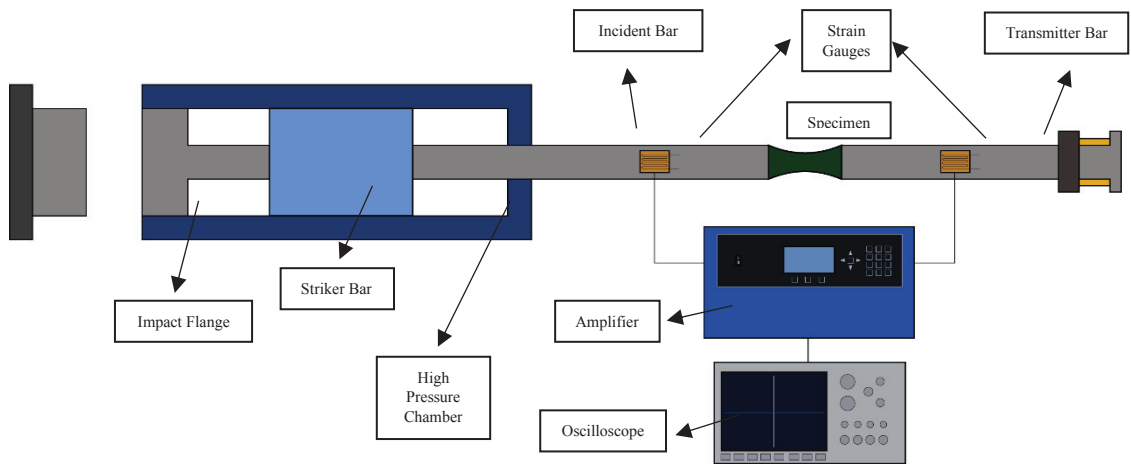


Figure 3.10. The schematic of TSHPB

The used TSHPB set-up was made of 316L stainless steel. The diameter of the incident and transmitter bar was 20 mm and the length 2.4 m. The elastic modulus of the bars (E_b) was 193 GPa and the density 7990 kg m⁻³. The stress waves on the bars were measured by using 350 Ω foil strain gages in a full Wheatstone-bridge configuration. The bridge voltage was recorded by an oscilloscope and amplifier (Figure 3.11). The velocity of the striker bar was determined with a laser-velocity gate mounted at the exit of the pressure vessel.

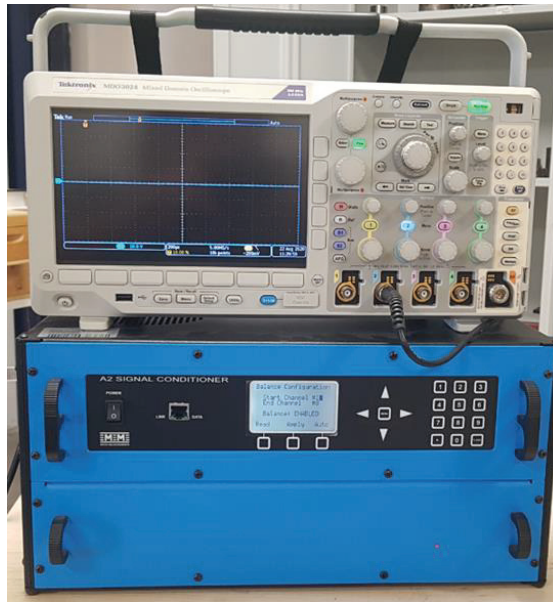


Figure 3.11. Picture of oscilloscope and amplifier

In order to avoid wave reflections from the test fixture, a test fixture composing of two parts was designed within the thesis (Figure 3.12). The test fixture was machined from the same material with that of the bars. The first part of the test fixture included the bolted connections and used to fixed the sample to the incident bar (Figure 3.13). A designed clamp jig shown in Figure 3.14 was used to connect the test sample to the transmitter bar. The sample was fixed to the transmitter bar by four bolts. The cross-sectional area on the fixture parts was equal and fixed at 314 mm^2 . Tests were recorded with a Fastcam Photron high speed camera with 60000 fps as shown in Figure 3.15. Two sources of light and a reflector were used to get images at such high fps. A high speed camera was connected to an oscilloscope with TRIG TLL IN cable to start simultaneous the time for the data and image acquisition.

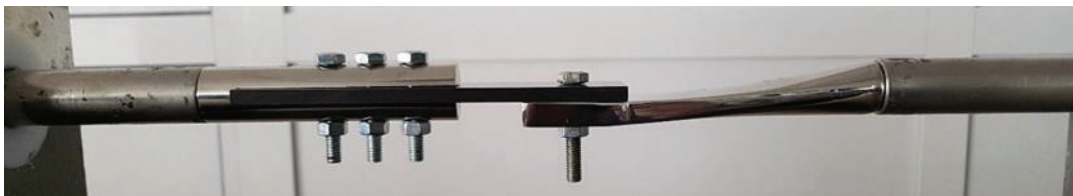


Figure 3.12. Picture of dynamic tests specimen fixed to apparatuses

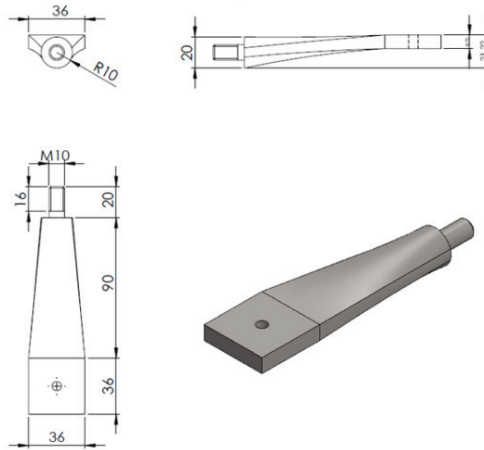


Figure 3.13. Technical drawing of TSHPB incident bar fixture apparatus

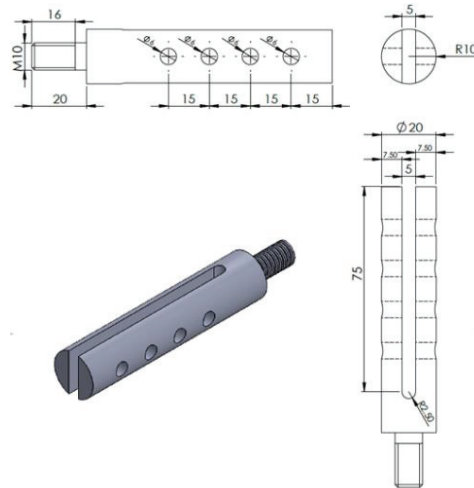


Figure 3.14. Technical drawing of TSHPB transmitter bar clamp apparatus



Figure 3.15. TSHPB bearing test set up

The strain on the bars was calculated as,

$$\varepsilon(t) = \frac{2V(t)}{K_{gain}V_{exc}GF(1 + \nu)} \quad (3.6)$$

where, V is the voltage read, V_{exc} is the excitation voltage, K_{gain} is the gain value, GF is the gage factor and ν is Poisson's Ratio of the bar material. The strain ($\varepsilon_s(t)$), stress ($\sigma_s(t)$) and strain rate ($\dot{\varepsilon}_s$) of the specimen were calculated as,

$$\varepsilon_s(t) = -\frac{2C_b}{L_s} \int_0^t \varepsilon_r(t) dt \quad (3.7)$$

$$\sigma_s(t) = \frac{A_b}{A_s} E_b \varepsilon_t(t) \quad (3.8)$$

$$\dot{\varepsilon}_s = -\frac{2C_b}{L_s} \dot{\varepsilon}_r(t) \quad (3.9)$$

where L_s is the length of the specimen, $\varepsilon_r(t)$ is strain data from the reflected bar, $\varepsilon_t(t)$ is strain data from the transmitter bar, A_b is cross-sectional area of the bar, A_s is cross-sectional area of specimen, E_b is elastic modulus of the bar and C_b is elastic wave speed of the bar material which can be formulated as,

$$C_b = \sqrt{\frac{E_b}{\rho_b}} \quad (3.10)$$

The SHPB tests were performed at 12.68 m s⁻¹ striker bar velocity. Tests were conducted without washers and 2.5 Nm and 10 Nm preloads were applied as with the quasi-static bearing test.

CHAPTER 4

NUMERICAL STUDY

4.1 MAT_162 Material Model

The MAT_162 composite material model in the Ls-Dyna was developed to simulate the progressive failure in unidirectional and woven fabric composites at high strain rates. The model can predict the fiber and matrix failure and delamination. The MAT_162 is based on the Hashin's failure criteria ⁷ and the Matzenmiller damage mechanics ²⁸. The tension-shear fiber failure mode f_1 , compression fiber failure mode f_2 and crush failure mode f_3 are sequentially given as

$$f_1 - r_1^2 = \left(\frac{E_a \langle \varepsilon_a \rangle}{S_{aT}} \right)^2 + \left(\frac{G_{ab}^2 \varepsilon_{ab}^2 + G_{ca}^2 \varepsilon_{ca}^2}{S_{FS}^2} \right) - r_1^2 = 0 \quad (4.1)$$

$$f_2 - r_2^2 = \left(\frac{E_a \langle \dot{\varepsilon}_a \rangle}{S_{aC}} \right)^2 - r_2^2 = 0 \quad (4.2)$$

$$f_3 - r_3^2 = \left(\frac{E_c \langle -\varepsilon_c \rangle}{S_{FC}} \right)^2 - r_3^2 = 0 \quad (4.3)$$

where a , b and c denote the in-plane and through thickness directions respectively. S_{aT} and S_{aC} are sequentially the compressive and tensile strengths in a direction and S_{FS} and S_{FC} are the fiber direction shear and crush failure, respectively. $r_j = 1, 2, 3$ denotes the damage state which has the initial value of 1 and updated with damage accumulation. In above equations, $\dot{\varepsilon}_a$ is

$$\dot{\varepsilon}_a = -\varepsilon_a - \frac{\langle E_c \varepsilon_c - E_b \varepsilon_b \rangle}{2E_a} \quad (4.4)$$

Three matrix damage modes, f_4 , f_5 and f_6 represent sequentially the transverse compressive matrix mode, perpendicular matrix mode and parallel matrix mode (delamination) and given as

$$f_4 - r_4^2 = \left(\frac{E_b \langle -\varepsilon_b \rangle}{S_{bc}} \right)^2 - r_4^2 = 0 \quad (4.5)$$

$$f_5 - r_5^2 = \left(\frac{E_b \langle \varepsilon_b \rangle}{S_{bT}} \right)^2 + \left(\frac{G_{bc} \varepsilon_{bc}}{S_{bc0} + S_{SRB}} \right)^2 + \left(\frac{G_{ab} \varepsilon_{ab}}{S_{ab0} + S_{SRB}} \right)^2 - r_5^2 = 0 \quad (4.6)$$

$$f_5 - r_5^2 = S^2 \left\{ \left(\frac{E_c \langle \varepsilon_c \rangle}{S_{cT}} \right)^2 + \left(\frac{G_{bc} \varepsilon_{bc}}{S_{bc0} + S_{SRC}} \right)^2 + \left(\frac{G_{ca} \varepsilon_{ca}}{S_{ca0} + S_{SRC}} \right)^2 \right\} - r_6^2 = 0 \quad (4.7)$$

where, S_{bT} and S_{cT} are the in-plane and transverse tensile strength, respectively. S_{ab0} , S_{bc0} and S_{ca0} are the shear strength of the corresponding planes (S_{ab0} represents the shear strength of ab plane). S is a scale factor that can be determined by fitting the analytical predictions to the experimental data for the delamination area. Under compressive strain, the damage surface is considered to be “closed”, and the shear strengths are assumed to depend on compressive normal strains based on the Mohr-Coulomb theory as $S_{SRB} = E_b \tan(\varphi) \langle -\varepsilon_b \rangle$ and $S_{SRC} = E_c \tan(\varphi) \langle -\varepsilon_c \rangle$, where, φ represents the material constant. S_{SRB} and S_{SRC} are the dependent shear strengths at in-plane transverse and out-of-plane directions respectively.

In the MAT_162, the damage softening parameter m_1 controls the tensile and compressive fiber failure mode in fiber direction in a unidirectional lamina model. m_2 controls the transverse compressive matrix failure mode in the transverse direction. m_3 is the softening parameter related to fiber crush mode and m_4 is for both perpendicular and parallel matrix mode. The effect of strain rate on the strength is formulated as

$$\frac{X_{RT}}{X_0} = 1 + C_{rate} \ln \left(\frac{\dot{\varepsilon}}{\dot{\varepsilon}_0} \right) \quad (4.8)$$

where, X_{RT} is the property at a strain rate of $\dot{\varepsilon}$ and X_0 is the property at the reference strain rate of $\dot{\varepsilon}_0$. C_{rate} is the rate sensitivity of the property. The reference strain rate is usually taken as 1 s^{-1} . The effect of strain rate on the strength properties is formulated as

$$\{S_{RT}\} = \{S_0\} \left(1 + C_{rate1} \ln \left(\frac{\{\dot{\epsilon}\}}{\dot{\epsilon}_0} \right) \right) \quad (4.9)$$

where, C_{rate1} is the strength rate sensitivity, $\{S_{RT}\}$ is the material strength and $\{S_0\}$ is the material strength at $\dot{\epsilon}_0$. The strain rate depended moduli are given as

$$\{E_{RT}\} = \{E_0\} \left(1 + C_{rate} \ln \left(\frac{\{\dot{\epsilon}\}}{\dot{\epsilon}_0} \right) \right) \quad (4.10)$$

where $\{E_{RT}\}$ is the elastic modulus and $\{E_0\}$ is the elastic modulus at the reference strain rate $\dot{\epsilon}_0$. C_{rate2} is rate sensitivity of the in-plane moduli, E_a and E_b ; C_{rate4} strain rate sensitivity of through thickness modulus, E_c and C_{rate3} strain rate sensitivity of the shear modulus G_{ab} , G_{bc} , and G_{ca} .

Eroded elements are considered as failed and removed from the analysis. In the MAT_162, elements can be eroded one of three ways. If the axial tensile strain is greater than E_LIMIT; if the compressive volume in an element is smaller than ECRSH and if the relative volume is greater than EEXPN, the element will erode. The MAT_162 material model parameters are listed in Table 4.2.

The MAT_162 material model parameters of the tested unidirectional carbon fiber reinforced epoxy composite were previously investigated in ref.²⁹ and tabulated in Table 4.3. The same model parameters were used in the models except additional calibration of EEXPN parameter was carried out and the resultant parameter was used as erode criteria for this study.

Table 4.2. MAT_162 material parameter explanations.

EA	Young's modulus longitudinal direction	SAB	Matrix mode shear strength - ab plane
EB	Young's modulus transverse direction	SBC	Matrix mode shear strength - bc plane
EC	Young's modulus through thickness direction	SCA	Matrix mode shear strength - ca plane
PRBA	Poisson's ratio – ba plane	SSFC	Scale factor for residual compressive strength
PRCA	Poisson's ratio – ca plane	AMODEL	1: Unidirectional lamina model 2: Fabric lamina model
PRCB	Poisson's ratio – cb plane	PHIC	Coulomb friction angle for matrix and delamination failure
GAB	Shear modulus – ab	E_LIMIT	Element eroding axial strain
GBC	Shear modulus – bc	S_DELM	Scale factor for delamination criterion
GCA	Shear modulus – ca	OMGMX	Limit damage parameter for elastic modulus reduction
SAC	Longitudinal tensile strength	ECRASH	Limit compressive relative volume for element eroding
SBT	Transverse tensile strength	EEXPN	Limit expansive relative volume for element eroding
SBC	Transverse compressive strength	AM1	Coefficient for strain softening property for fiber damage in a direction
SCT	Through thickness tensile strength	AM2	Coefficient for strain softening property for transverse compressive matrix failure mode in b direction (unidirectional)
SFC	Crush strength	AM3	Coefficient for strain softening property for fiber crush and punch shear damage
SFS	Fiber mode shear strength	AM4	Coefficient for strain softening property for matrix failure and delamination damage
SAT	Longitudinal tensile strength		

Table 4.3. Unidirectional Carbon/Epoxy MAT_162 parameters ²⁹.

RO (kg/m³)	EA (GPa)	EB (GPa)	EC(GPa)	PRBA	PRCA	PRCB	GAB (GPa)
1487.5	122.51	8.4	8.4	0.10	0.20	0.20	4.76
GBC (GPa)	GCA (GPa)	SAT (MPa)	SAC (MPa)	SBT (MPa)	SBC (MPa)	SCT (MPa)	SFC (MPa)
1.5	1.5	1835.4	700	40.5	184.2	80	2500
SFS (MPa)	SAB (MPa)	SBC (MPa)	SCA (MPa)	SSFC	AMODEL	PHIC	E_LIMIT
405	41.5	55	55	0.35	1	10	0.005
S_DELM	OMGMX	ECRASH	EEXPN	AM1	AM2	AM3	AM4
1.2	0.999	0.8	1.10	1.0	0.001	0.5	0.3

4.2. Modelling Methodology

Three dimensional components of the models were designed in Solidworks and saved as .IGS files. The test samples and quasi-static test set up were meshed with quad elements while the TSHPB bars were meshed with tetrahedron elements using Hypermesh Software. Tested unidirectional composite structure consists of 66 equivalent plies, each modeled and meshed separately and combined with DubNod card in the LS-PrePost software. All plies were assembled with no penetration. Boundary conditions, material properties, contacts, mass-scaling and termination time were defined with LS-PrePost software. The three dimensional models were solved with non-linear explicit FE code of LS-Dyna Solver.

A meso-level approach was adopted where each composite ply was modeled separately to increase the accuracy of the model. The specimen's ply count was determined with microscopic inspection and created using 66 layers and combined with a DubNod card in Ls-PrePost. The DubNod card allows the merging the nodes within a certain distance and combines all of the plies as one bulk specimen. AUTOMATIC_SINGLE_SURFACE contact card was used to provide interaction between plies. The specimen was meshed with a different strategy in which fine meshes were used around the hole while coarser meshes were used at the edges. (Figures 4.1(a) and (b)). This meshing method increased the CPU calculation times. The specimen was created with 110000 solid stress elements and 119000 nodes. A 36x75 mm area similar to the quasi-static tests was restricted with SPC_SET card. This card allows the chosen nodes to be restricted in any directional or rotational movement. These nodes are restricted in translational x, y and z direction and rotational x, y and z axis.

The quasi-static test fixture was modelled in a detailed manner to simulate the frictional force more accurately (Figure 4.2(a)). The test fixture was modelled using 5700 solid elements with MAT020_RIGID material model ($E=210$ GPa and $\nu=0.3$). The movement of the apparatus was restricted in translational y and z direction and rotational x, y and z axis. The velocity of the apparatus in x-direction was kept constant by the PRESCRIBED_MOTION_RIGID card according to the reference test ($3.33 \times 10^{-5} \text{ m s}^{-1}$). Static friction coefficient 0.1 and dynamic friction coefficient 0.01 was used for the quasi-static model. The bolt model is shown in Figure 4.2(b). The bolt was modelled with 18000

constant stress elements using MAT001_ELASTIC ($E=210$ GPa and $\nu=0.33$). AUTOMATIC_SURFACE_TO_SURFACE card was used to ensure contact between bolt-specimen, bolt-apparatus and specimen-apparatus. No restrictions were used to confine the bolt movement.

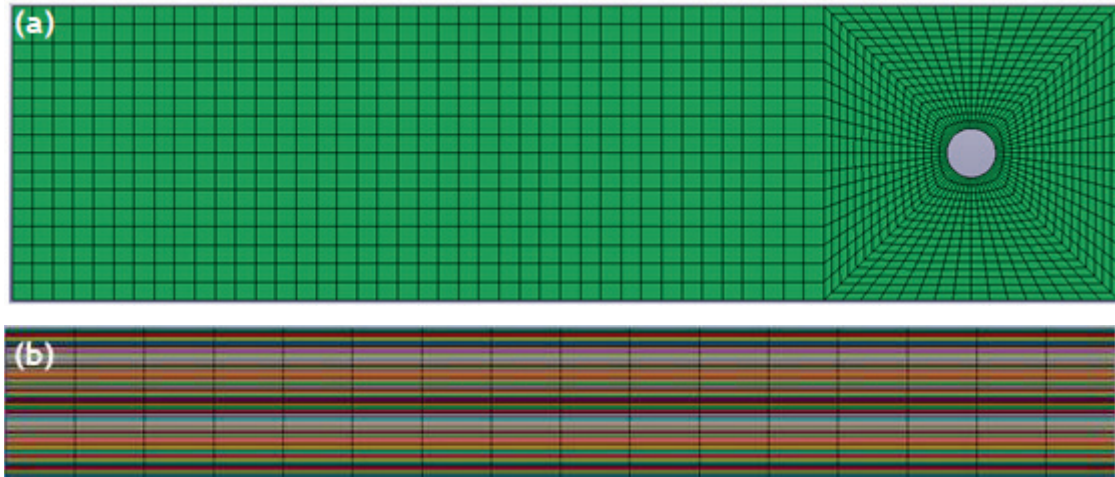


Figure 4.1. Quasi-static model specimen (a) top view (b) side view

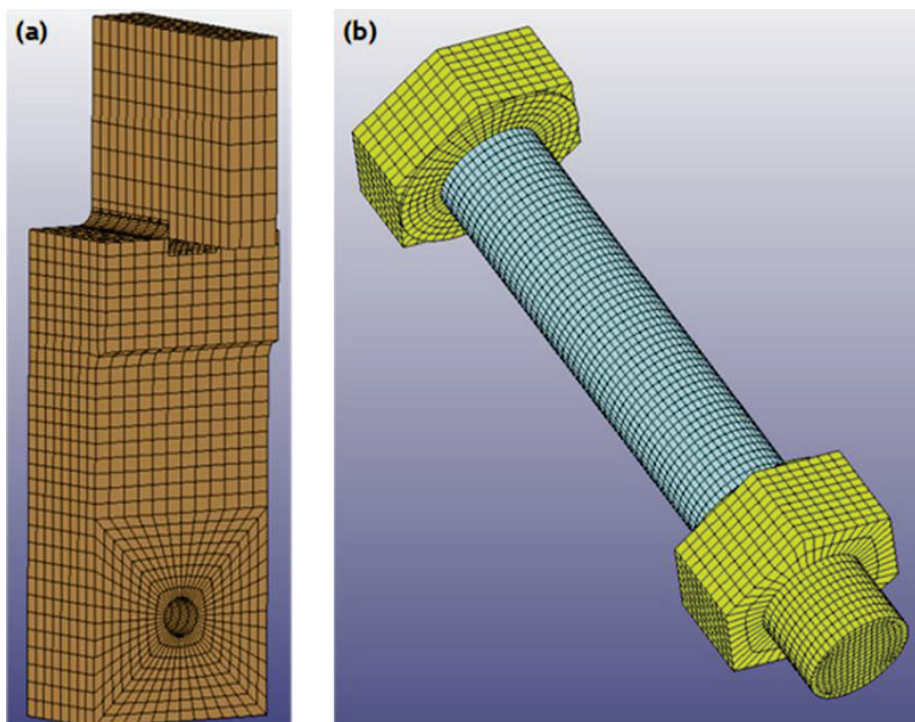


Figure 4.2. Quasi-static model isometric view of (a) apparatus and (b) bolt

Figures 4.3 (a-c) represent isometric views of the numerical model of the quasi-static bearing test set-up. Since the total CPU time for the quasi-static test solutions were relatively long, the mass scaling was applied by defining a positive time step in CONTROL_TIMESTEP card. In order to determine the mass scaling factor, the simulation was initially run without mass scaling, and the determined time step without mass scaling was multiplied by 10, 100 and 1000 until internal energy became comparatively higher than kinetic energy. Mass scaling with 10000 multiplication was used for this model.

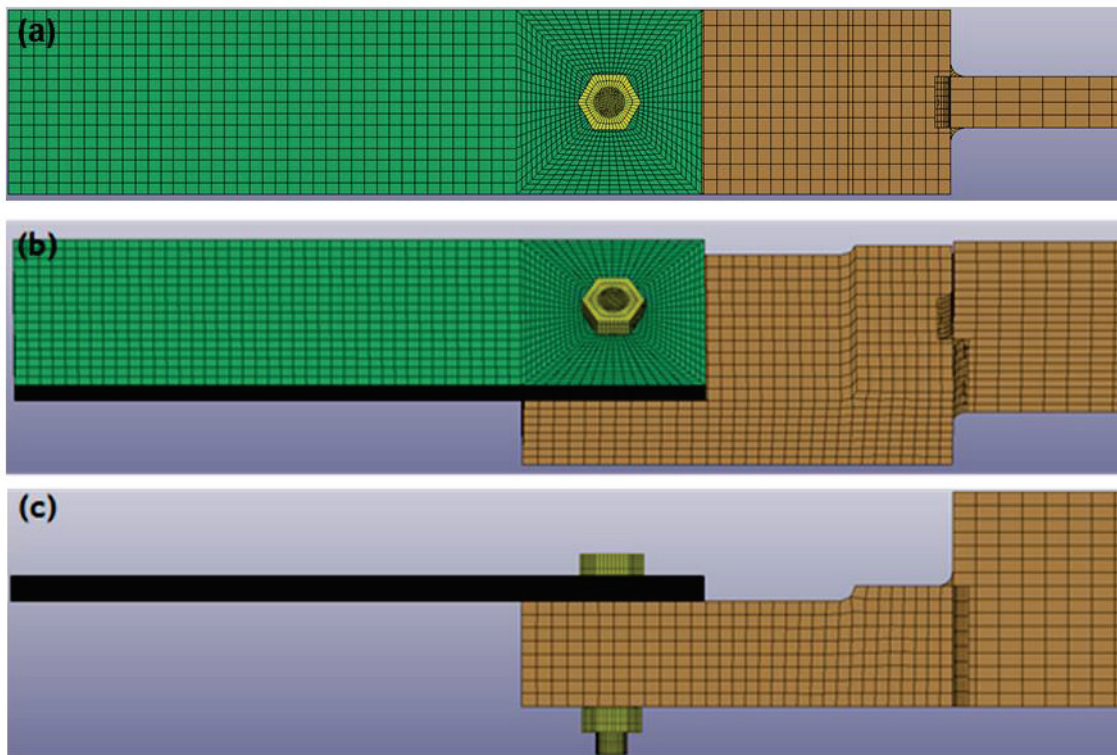


Figure 4.3. Quasi-static model (a) top view (b) isometric view and (c) side view

The TSHPB model are shown in Figures 4.4(a-c). The length of the incident and the transmitter bar were taken the same as the experiments, 2.4 meter. The test apparatus and the bars were modelled with tetrahedron elements. The incident and the transmitter bars were modelled with 97600 and 325903 elements, respectively. The 316L bars were modeled with MAT001_ELASTIC ($E=193$ GPa and $\nu=0.33$) material model. Movement of the bars were restricted in translational y and z direction and rotational x, y and z axis

with the SPC_SET card. An additional restriction was implemented to nodes at the transmitter bar's free end to immobilize the bar. Two different mobilization method were used to give the incident bar a velocity. First method was giving the exact test velocity 12.68 m s^{-1} to the incident bar with PRESICRIBED_MOTION_SET card in LS-PrePost. Second method was implementing a pulse taken from reference test to the incident bar's free end with SEGMENT_SET card in LS-PrePost. The clamp bolts were converted to pins in the dynamic model since the clamping force has no effect on overall results. The bolt was modeled with 8352 and the clamp pins 2304 elements. The bolt and the clamp pins are modeled with MAT001_ELASTIC ($E=210 \text{ GPa}$ and $\nu=0.33$) material model. AUTOMATIC_SURFACE_TO_SURFACE card was used to ensure the contact between the bolt-specimen, bolt-incident bar, clamp pins-transmitter bar and specimen-transmitter bar. The dynamic model specimen was completely fine meshed to accurately observe the crack propagation (Figures 4.4(a-c)). The specimen contained 66 separate plies that were merged with DubNod card in Ls-PrePost. The specimen has a total of 390720 solid stress elements. The static and dynamic friction coefficients between the specimen and the incident bar were taken 0.1 and 0.01, respectively. AUTOMATIC_SINGLE_SURFACE contact card was used to create an interaction between plies.

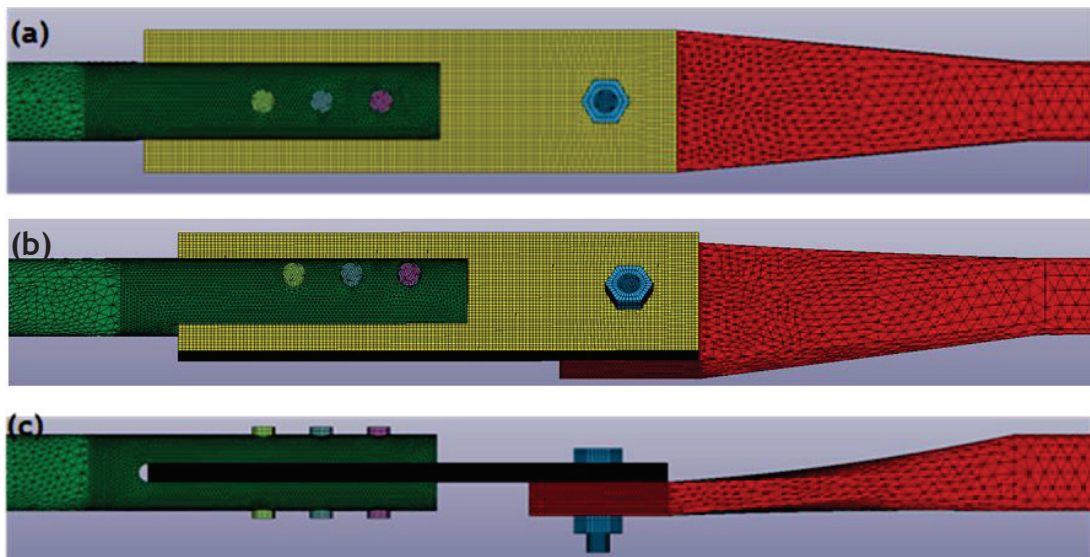


Figure 4.4. Dynamic model (a) top view (b) isometric view and (c) side view

CHAPTER 5

RESULTS AND DISCUSSION

5.1. Quasi-static Bearing Test Results

The force-displacement curves of the quasi-static bearing tests at $3.33 \times 10^{-5} \text{ m s}^{-1}$ and 2.5 Nm bolt torque are shown in Figures 5.1. The force in the same figure is drawn as function of the extensometer and stroke displacement for comparison. The difference between the extensometer and the stroke displacements seen in the same figure is resulted from the difference in the gage lengths. The video extensometer markers were placed according to the ASTM D5961, one marker was placed on the rear surface of the specimen and other marker on the fixture rear surface with a constant gage length of 15 mm. While, the stroke displacement was measured along the fixture and the specimen and hence the gage length is much bigger. The force-displacement curves exhibit two peak forces which is presumed a characteristic of a unidirectional composite specimen. These peak forces are marked by the circles in Figure 5.1. As clearly seen in the deformed pictures of a tested sample at different deformation times in Figures 5.2(a-d), the first peak force results from the initiation of the first crack parallel to the fiber direction and the second peak force is resulted from the initiation of the second crack which leads to a catastrophic failure. The values of the first peak force are 5168, 4818 and 5500 N with an average value of 5162 N and the values of the second peak force are 6377, 5411 and 6855 N with an average value of 6214 N. There are 23.39%, 12.3% and 24.63% force increment between the initiation of the first and the second cracks, respectively. The bearing tests of composite specimens resulted in two different deformation regions. The first crack starts at a location where the bolt shank contacts with the specimen's hole and the second crack is formed at the opposite side of the bolt shank's contact surface and proceeds slowly with increasing load (Figures 5.2(a-d)). Unidirectional composites of joints in which the bearing force applied parallel to fiber direction fractures parallel to the fiber

direction ²⁴. The failure occurs with two parallel cracks, which is called a shear-out deformation. Unlike the shear-out deformation mode, the failure of the tested joint occurs slowly with losing the load carrying capacity. The initial lower slope in the force-displacement curves shown in Figure 5.3 is partly due to the static frictional forces between the specimen and fixture and partly due to the gap between the bolt and the specimen hole. In this stage, the force increases to 382, 375 and 613N respectively with a steep slope. Extensometer was not able to capture the minor changes of the bolt displacement. The bolt is fully loaded in the region ii of Figure 5.3.

The force-displacement curves of the quasi-static bearing tests at $3.33 \times 10^{-5} \text{ m s}^{-1}$ and 10 Nm torque are shown in Figures 5.4, together with a representative force-displacement curve of the tests at the same velocity and 2.5 Nm torque. Again two peak forces are seen; the values of the first peak force are 5055, 5000 and 6494 N and the second peak force 6553, 6202 and 6144 N. The first two tests show 31.06% and 22.7% increase but the third test show a 5.11% decrease between the first and second peak force. The average of the first peak is 5162 N for 2.5 Nm and 5516 N for 10 Nm and the average of the second peak is 6214 N for 2.5 Nm and 6300 N for 10 Nm. These results show that the preload is effective in increasing the first peak force but has almost no effect on the second peak force. This is expected, because when the first crack is formed, the bolt relaxes and the effect of preloading is largely removed. In the literature, increasing bolt torque always results with an increasing load carrying capacity for the composite bolted joints ¹ because increasing bolt torque causes an expansion on the bolt's load effective area which lowers the stress localization. As the torque of the bolt increases, the minimum force to overcome the static friction is increased as well and these forces were 1016, 1333 and 1050 N respectively with an average of 148% increase compared to 2.5 Nm quasi-static test at the same velocity. As stated in the literature, giving excessive amount of torque to a bolt can cause premature microcracks on the matrix ¹². Unidirectional composites are more vulnerable to excessive preload because an excessive pressure mostly deforms the matrix which is the primary deformation component. On unidirectional composite samples over more than 15 Nm bolt torque initiated a crack without any other force.

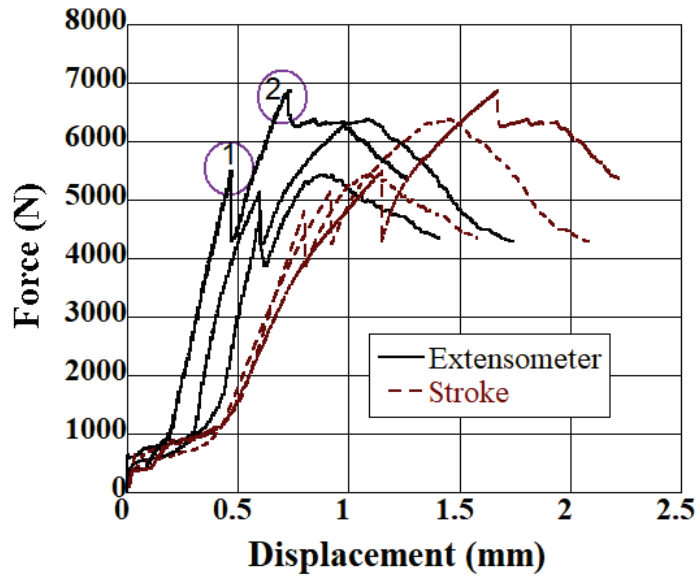


Figure 5.1. The force-displacement curves of quasi-static bearing tests at $3.33 \times 10^{-5} \text{ m s}^{-1}$ and under a bolt torque of 2.5 Nm

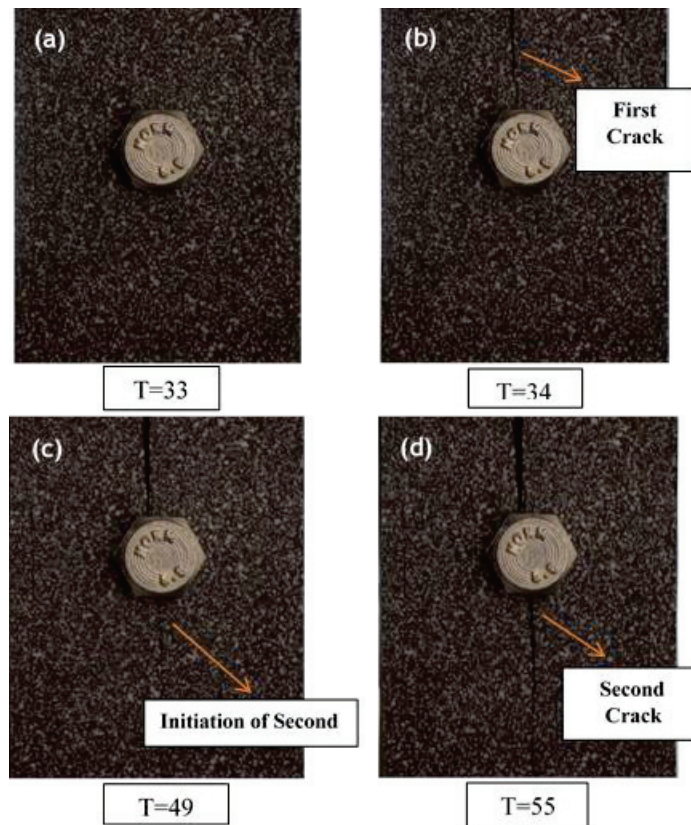


Figure 5.2 The deformation pictures of composite specimen at (a) 38th (b) 39th (c) 55th (d) 60th second of the quasi-static test, cross-head velocity of $3.33 \times 10^{-5} \text{ m s}^{-1}$ and bolt torque of 2.5 Nm

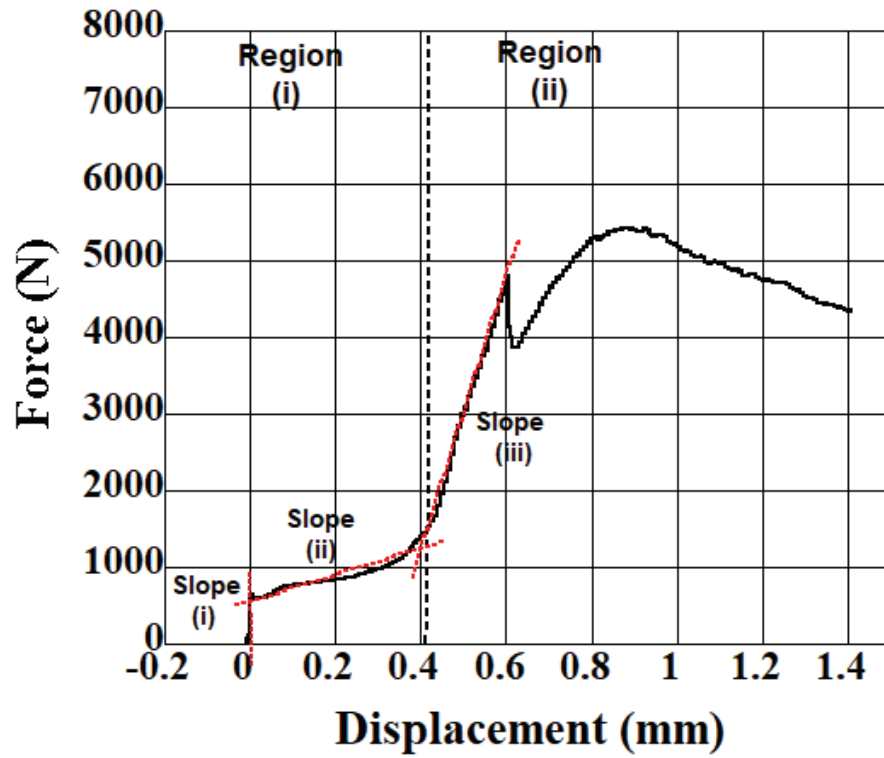


Figure 5.3. The division of force-displacement curves

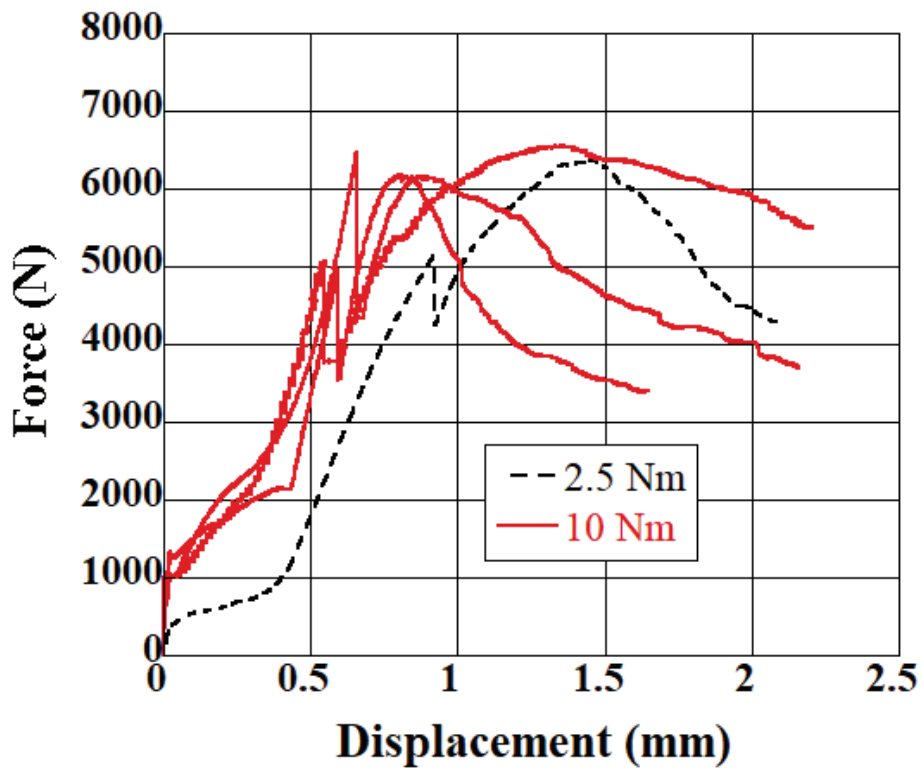


Figure 5.4. The force-displacement curves of quasi-static bearing tests at a loading velocity of $3.33 \times 10^{-5} \text{ m s}^{-1}$ and under a bolt torque of 10 Nm

The force-displacement (stroke displacements) curves of quasi-static bearing tests at $1.66 \times 10^{-3} \text{ m s}^{-1}$ and 2.5 Nm torque are shown in Figures 5.4 together with a representative force-displacement curve of the tests at $3.33 \times 10^{-5} \text{ m s}^{-1}$ and 2.5 Nm torque. Two specimens showed similar force-displacement curves and failure modes as with the tests at $3.33 \times 10^{-5} \text{ m s}^{-1}$ while one specimen showed a mixed deformation mode of cleavage and shear-out. The average of the second peak force of three tests is 6078 N which is slightly less than that of the tests at $3.33 \times 10^{-5} \text{ m s}^{-1}$, 6214 N. This shows almost no effect of loading rate at the quasi-static velocities. In the mixed deformation mode, the specimen shows three specific peak forces at the force-displacement curve. The locations of the cracks are shown in Figure 5.5. The first and second crack formation is very much similar to that of low velocity test. While the third crack occurs parallel to the first crack, forming a shear-out deformation mode. As numbered in Figure 5.4, the shearing out mode of failure, number 3, results in a sudden reduction of force. Note that the third crack is formed after the second crack and it combines with the first crack to form a shear out mode of failure. Similar results can be found in the literature as the loading velocity increase, it can alter the deformation mode^{17, 19}. The forces needed to overcome the static friction forces were found to be 575, 335 and 325N respectively similar to tests at $3.33 \times 10^{-5} \text{ m s}^{-1}$.

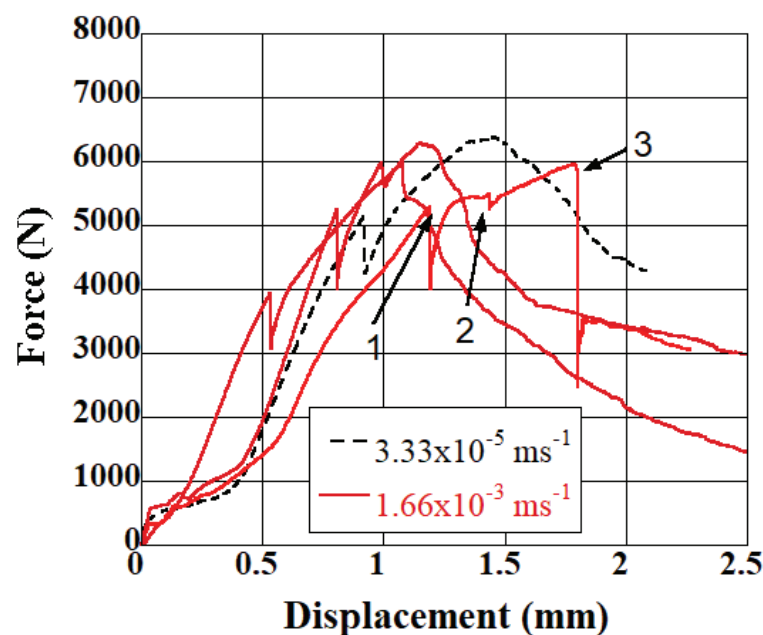


Figure 5.5. Quasi-static force-displacement curves with 2.5 Nm bolt torque and $1.66 \times 10^{-3} \text{ m s}^{-1}$ cross-head velocity

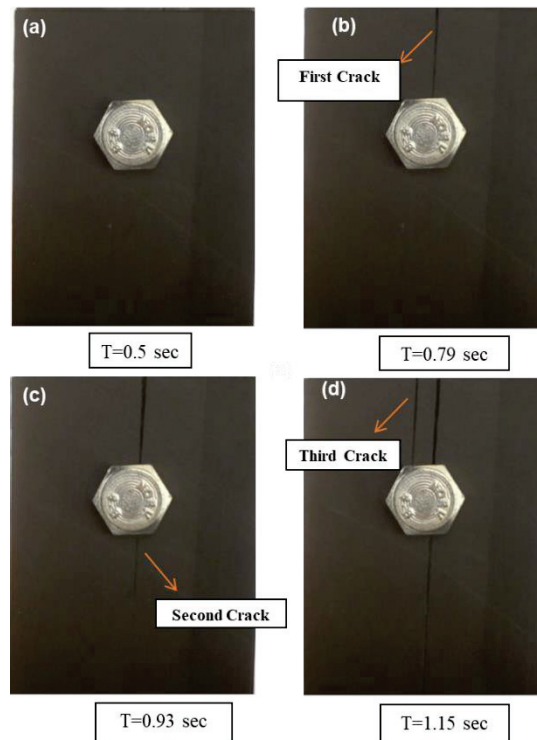


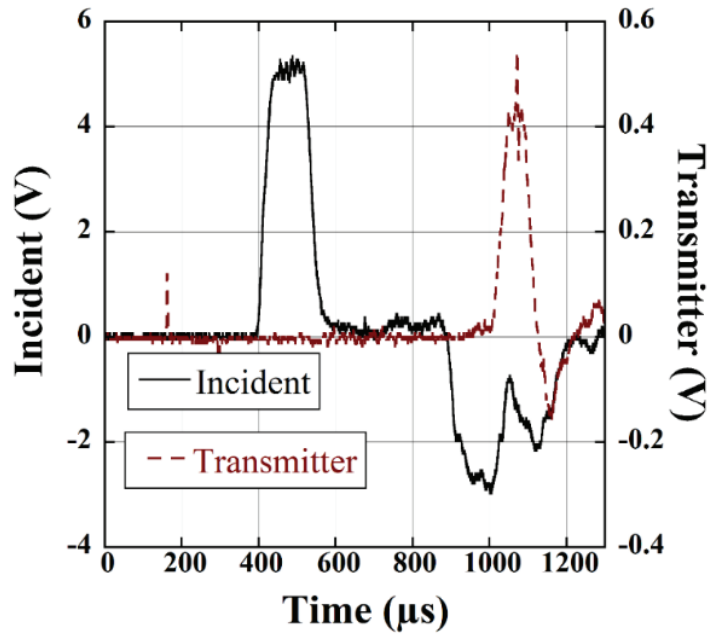
Figure 5.6. Deformation pictures of composite specimen at (a) 0.5th (b) 0.79th (c) 0.93th (d) 1.15th second of the quasi-static test, cross-head velocity of $1.66 \times 10^{-3} \text{ m s}^{-1}$

5.2. Dynamic Bearing Test Results

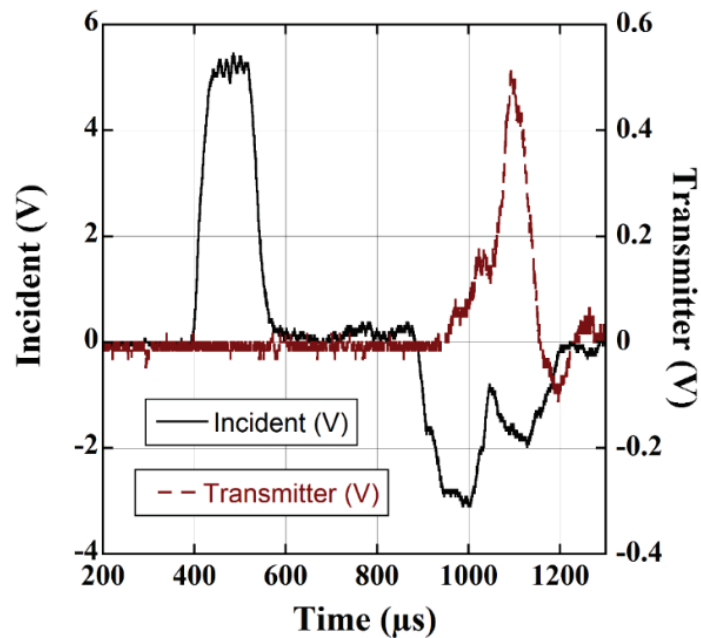
Two studies in the literature used TSHPB for dynamic testing of composite bolted joints^{24,25}. Both studies use a cylindrical apparatus, changing the specimen's dimensions. Designed apparatus for this study preserved the same dimensions and conditions of quasi-static tests and transferred the same conditions to TSHPB bearing tests. Conducted tests have an average of 59ms reflected-transmitter wave mismatch due to apparatus usage. This mismatch has been fixed with a change in the starting point of the reflected wave to the end of the transmitter wave. There were no other data correction methods used. The SHPB strain reading of incident, reflected and transmitter bars are shown in Figure 5.7(a) and (b) for 2.5 and 10 Nm torques, respectively. Figures 5.8(a) and (b) show the force displacement curves at 12.68 m s^{-1} and 3.3 m s^{-1} at 2.5 and 10 Nm, respectively. Different from quasi-static tests, all the TSHPB specimens tested at 2.5 Nm have the same deformation mode of shear-out as seen in Figure 5.9. Due to rapid velocity of loading, crack formations are not seen on the stress-strain curve. Three cracks are formed; the first

two cracks shape the shear-out deformation mode while the third crack causes the cleavage deformation mode. This deformation mode difference can be explained with the bolt's loose movement. During the beginning of the test, the incident bar being pulled along with the bolt created a sudden acceleration in velocity, causing the bolt to get clear of the friction forces and torque. Thus, the bolt hit the specimen and caused a shear-out deformation mode. After the second loading pulse, the bolt proceeded through the space created by the shear-out deformation mode, which expanded the specimen and caused the third crack that created a mixed shear-out, cleavage deformation mode. Some examples can be observed in the literature that indicate the effect of loading velocity on deformation mode^{17, 19, 20, 24}. Wang et al.²⁴ show that with an increasing strain rate, deformation mode tends more towards localized deformations. Bearing forces of the three tests were found to be 9833, 9800 and 8536 N at 2.5 Nm respectively with an average of 9389 N. The TSHPB tests result in higher forces than the quasi-static tests. This increase in bearing force was found to be around 51% by calculating the average peak forces of quasi-static and dynamic tests. An increase in bearing force with an increasing loading rate had been observed on some studies in the literature as well^{18, 24}. Although the results of this study are well agreed with some studies in the literature, some authors did not observe any increase in bearing force^{17, 20, 22, 23}. These controversial results can be explained with different strain rate dependencies of the composite components. Although the fibers do not have any dependency on strain rate, the matrix has properties dependent on strain rate²⁶ which is the reason for the 51% increase in bearing force. Different from the 2.5 Nm torqued bolt dynamic tests, all dynamic test specimens at 10 Nm bolt torque have the cleavage deformation mode as shown in Figure 5.10. The first crack starts from the contact point of the bolt shank and the specimen and then proceeds through the end of the specimen, parallel to the fiber direction. The second crack initiates from the rear of the bolt shank's contact area and proceeds through the clamped end of the specimen. Bearing force of two tests were found to be 10766 and 8866 N respectively with an average of 9816 N. Taking into consideration of the average bearing forces, 10 Nm dynamic tests have 4.5% increased bearing force compared to 2.5 Nm. This difference can be explained with the change in deformation mode. Unlike 2.5 Nm dynamic tests, all the specimens with 10 Nm bolt torque failed with a cleavage deformation mode. There are no other studies in the literature that covers the effect of the bolt torque with an increasing strain rate but this deformation change can be explained with the movement of the bolt. As the bolt torque increases, it restricts the bolt's movement. This restriction keeps the bolt on

the starting position, prevents the impact between the bolt and the specimen and causes the specimen to fail with a cleavage deformation mode. These results show that the applied torque increases the bearing force also at high velocity tests and drastically changes the deformation mode.

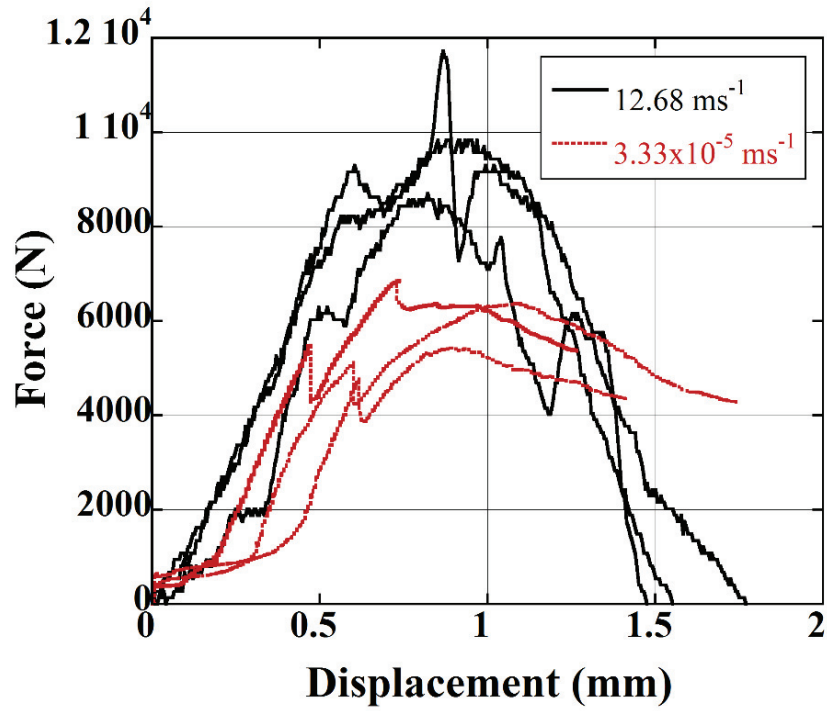


(a)

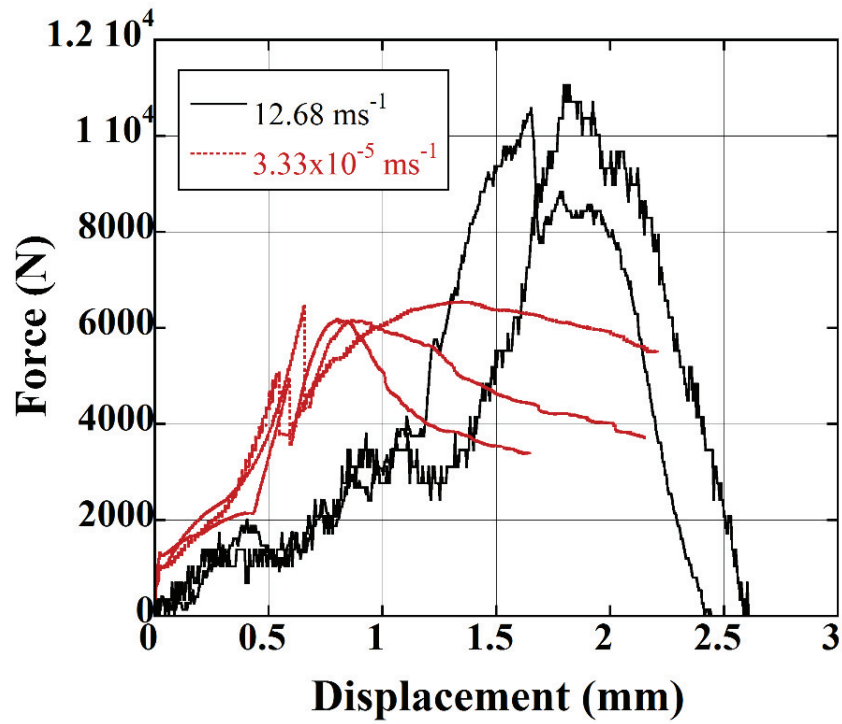


(b)

Figure 5.7. Incident, reflected and transmitter voltage readings of the tests at (a) 2.5 and (b) 10 Nm bolt torque



(a)



(b)

Figure 5.8. Force-displacement curves at 12.68 m s^{-1} and $3.33 \times 10^{-5} \text{ m s}^{-1}$ at (a) 2.5 and (b) 10 Nm bolt torque

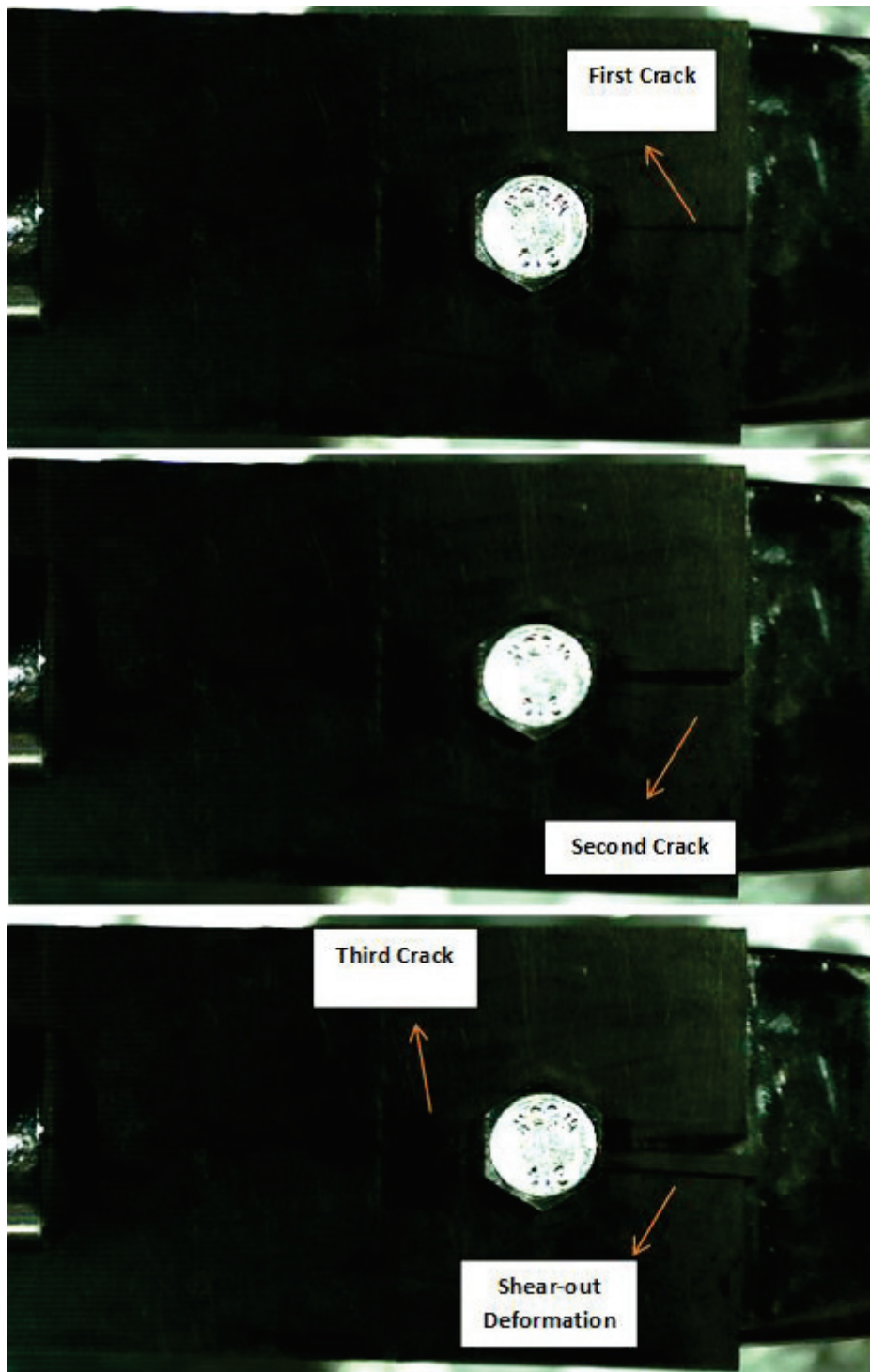


Figure 5.9. Deformation pictures of composite specimen after (a) 0.000033 (b) 0.000067 (c) 0.0001 second the dynamic test started, with loading velocity of 12.68 m s^{-1} and 2.5 Nm bolt torque

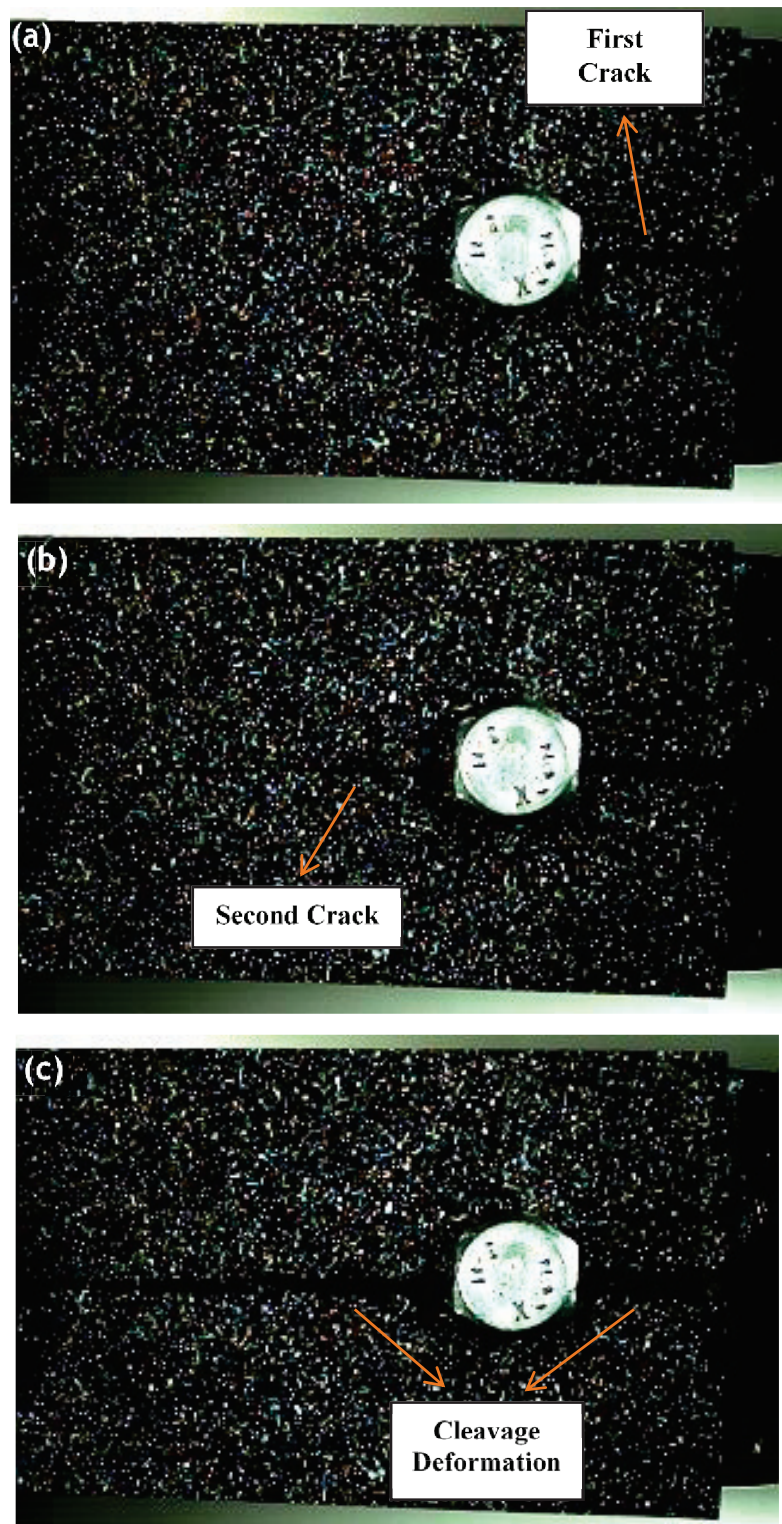


Figure 5.10. Deformation pictures of composite specimen after (a) 0.000033 (b) 0.000067 (c) 0.0001 second after the dynamic test started, with loading velocity of 12.68 m s^{-1} and 10 Nm bolt torque

5.3. Modelling Results

In the created quasi-static model, forces were taken from the bolt shank to specimen contact area and the bolt displacement taken from apparatus's covered distance through x direction. As a result of EEXPON calibration study (Figure 5.11), best fit was ensured with 1.003 value in terms of deformation mode and peak forces. The first peak of the model which is related to first crack formation was well agreed with the reference test results (2.5 Nm at $3.33 \times 10^{-5} \text{ m s}^{-1}$). The reference test has an average of 5366 N first peak force and the model has a 4463 N first peak force which shows a difference of 12.3%. At the second peak, tests have an average of 6025 N peak force and the model has an 8666 N peak force which shows a difference of 43.8%. This difference can be explained with difference between the deformation modes is due to the clamping method used in the model. Clamping was done with the restriction of all the nodes at the clamp area (75x36 mm) translational x, y and z direction and rotational x, y and z axis. This restriction caused a stress free zone at the clamped area, prevented the initiation of the perpendicular second crack. As a result, two diagonal cracks formed instead of one which increased the second peak force. The reason that the cracks did not follow the shortest path and formed diagonally can be explained with the stress localization through fiber direction. This localization can be seen on von Mises deformation Figure 5.14(b). In quasi-static tests, after the second peak force there was a slow decrease of force as the crack proceeded however in quasi-static model there was an abrupt decrease of force because of the way cracks formed which caused the specimen to lose the load carrying capacity suddenly. The created model showed no fiber damage. Perpendicular matrix mode (history variable #10) which indicates the deformation of the matrix in fiber and transverse direction. The location of the crack onset was well agreed with the tests. After the first crack occurred, forming of the side cracks can be seen on Figure 5.12 (b). When the diagonal cracks formed, a perpendicular stress wave started from the area where the second crack occurred in the reference tests (Figure 5.12 (c)).

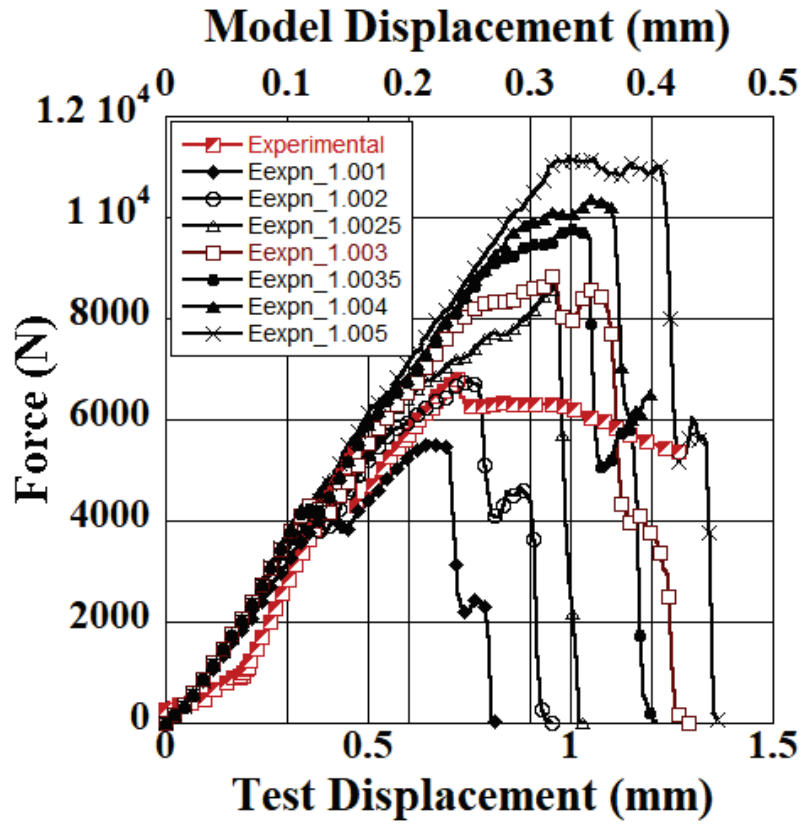


Figure 5.11. Comparison of quasi-static models with various EEXP values

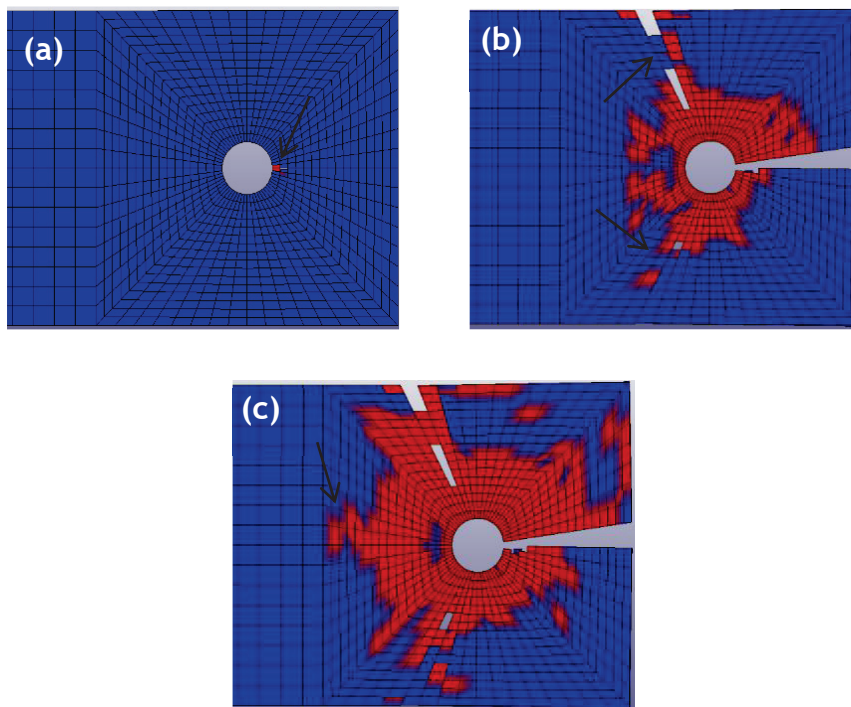


Figure 5.12. Deformation pictures of model history variable#10 (a) crack initiation (b) side cracks (c) perpendicular stress wave through fiber direction

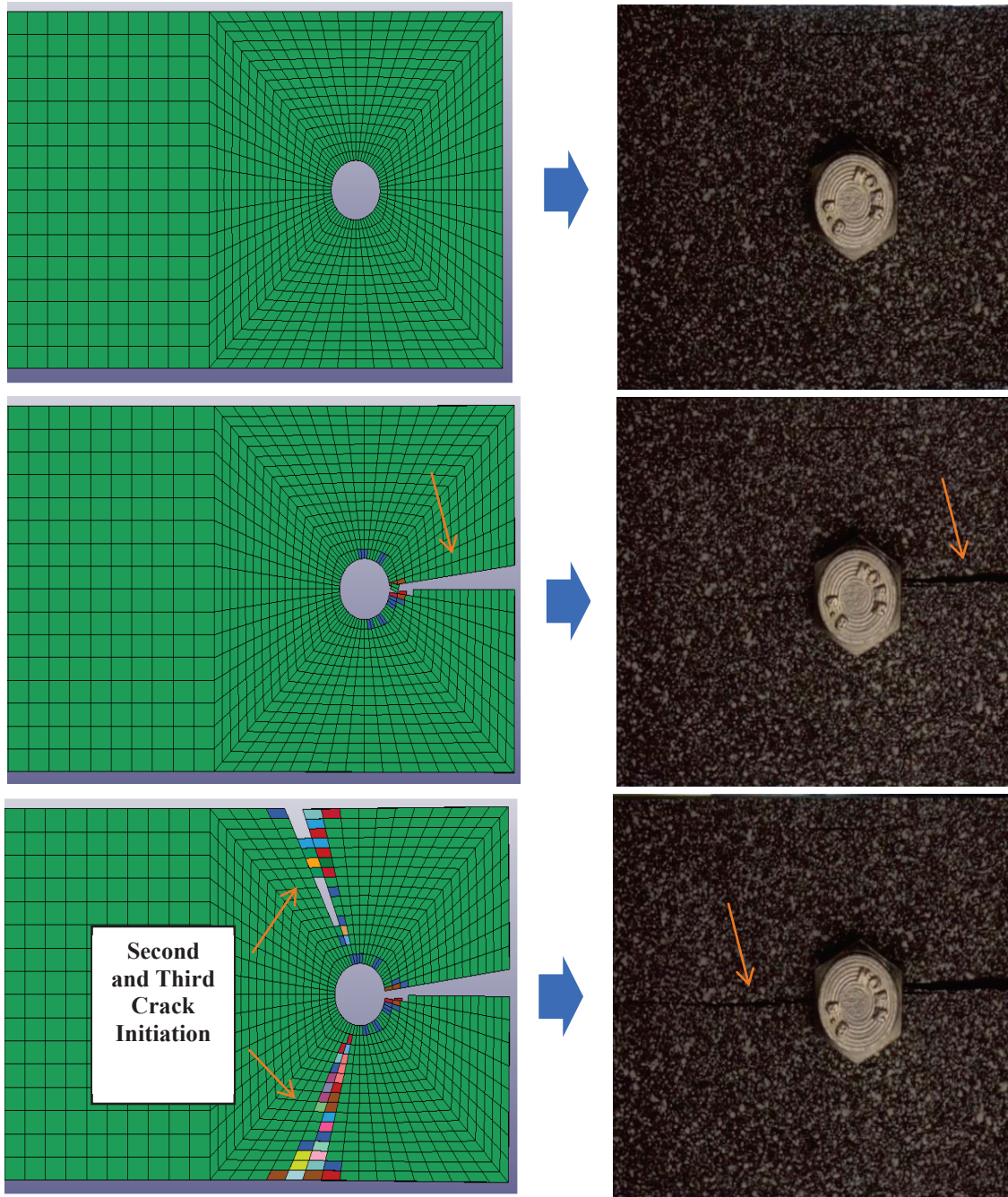


Figure 5.13. Numerical deformation pictures of the quasi-static model and corresponding test specimen

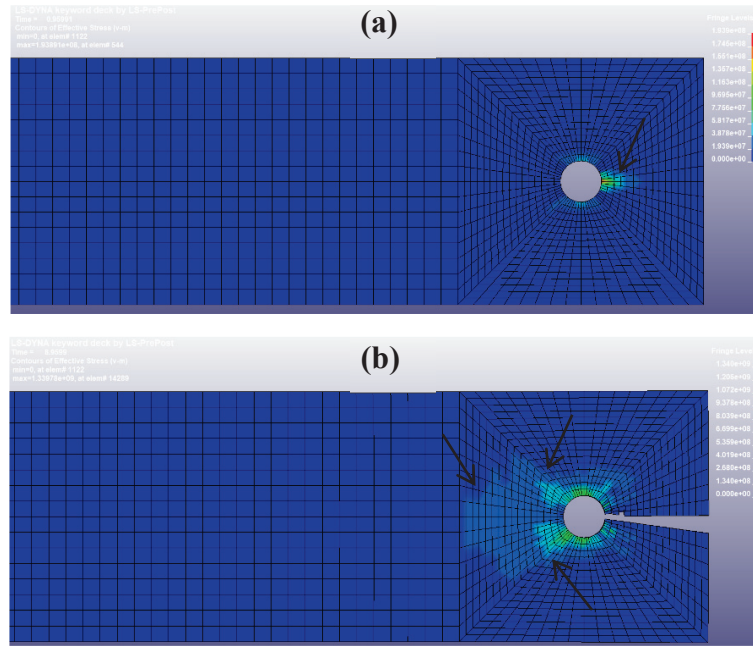


Figure 5.14. Von Misses deformation pictures of the quasi-static model (a) crack initiation (b) side cracks and perpendicular stress wave through fiber direction

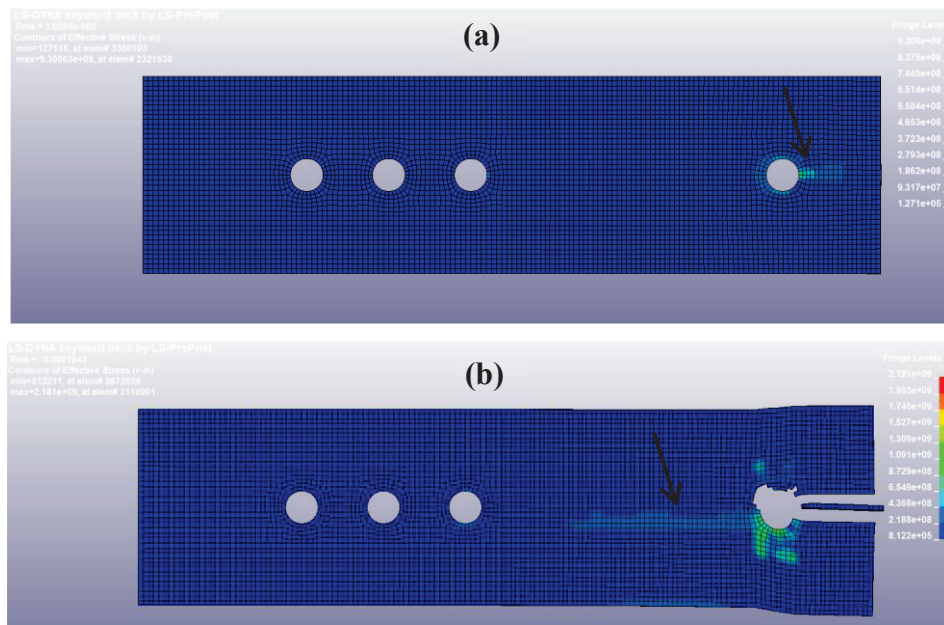


Figure 5.15. Von Misses deformation pictures of the velocity implemented dynamic model (a) crack initiation (b) perpendicular stress wave through fiber direction

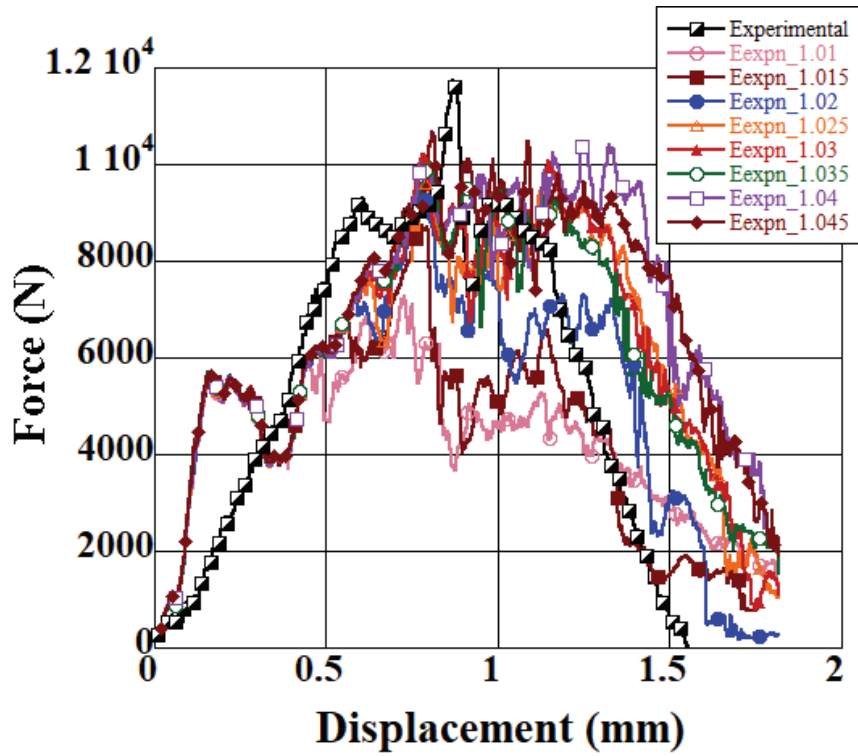


Figure 5.16. Comparison of dynamic models with various EEXPn values

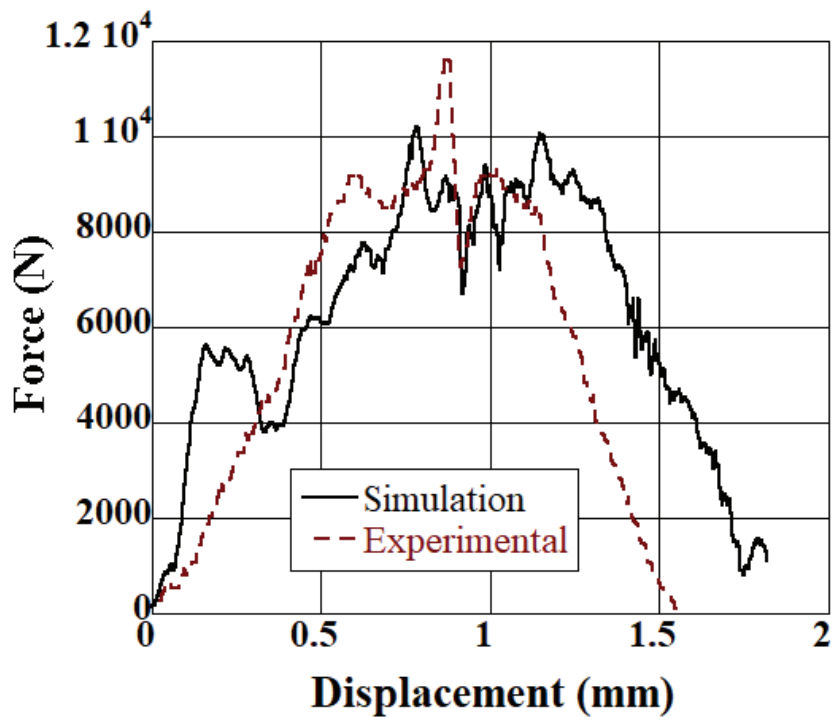


Figure 5.17. Comparison of dynamic reference test and velocity implemented numerical model

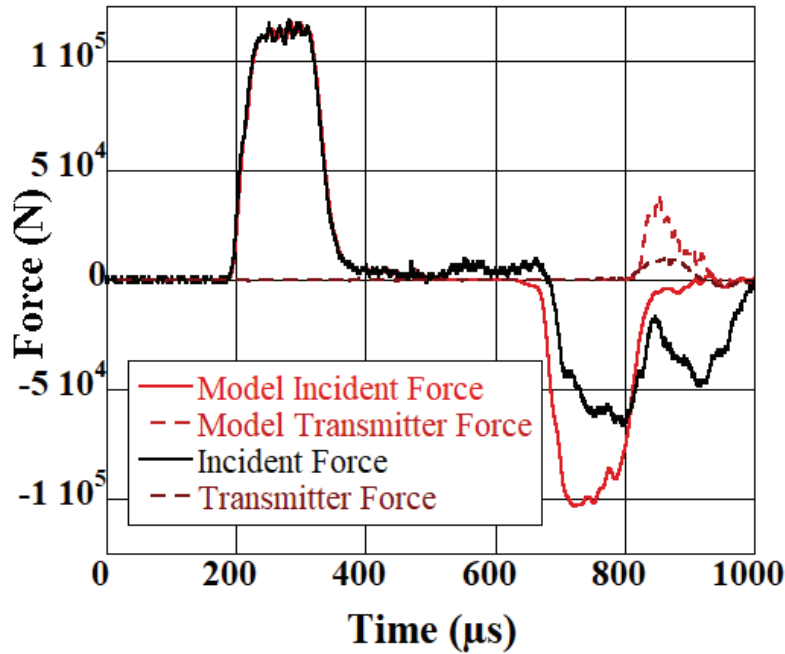


Figure 5.18. Comparison of pulse implemented dynamic model and the reference dynamic test

In the pulse implemented dynamic model, the movement has been achieved with a pulse taken from the reference test implemented on the free end of the incident bar. The force data of the model has taken from the elements located on same distance as the strain gauges on the incident and the transmitter bar. The force-time curve is given in Figure 5.18. The reference test and the model have an 10416 and 31944 N transmitter force respectively with three times of error. This error was mainly due to mesh type difference between the specimen and the bars. Due to complex shape of the grips, the bars and the grips meshed with triangular elements. The specimen meshed with tetrahedron elements. As the wave propagates through the incident bar to specimen, the stress wave was transferred from triangular elements to tetrahedron elements and triangular elements again. This wave transfer resulted with an inaccurate transmitter force nearly three times higher than the reference test. The deformation pictures of the model compared with the reference test have shown in Figure 5.20. Deformation mode of the pulse implemented model have better agreement with the reference test. Figure 5.20(d) shows a similar third crack propagation located on the middle of the specimen as the reference test.

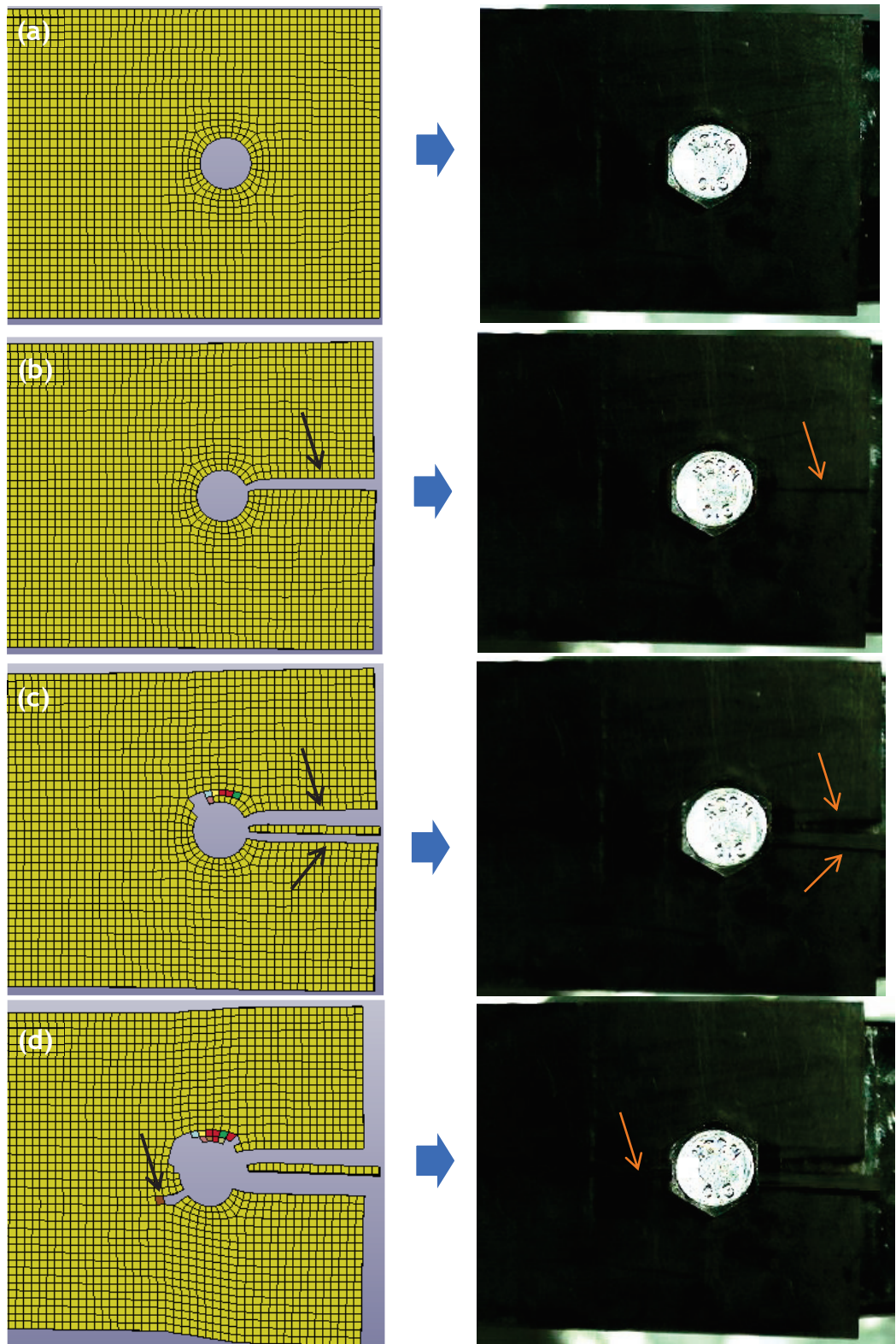


Figure 5.19. Deformation pictures of velocity implemented model (a) before crack initiation (b) first crack (c) shear out deformation mode (d) third crack

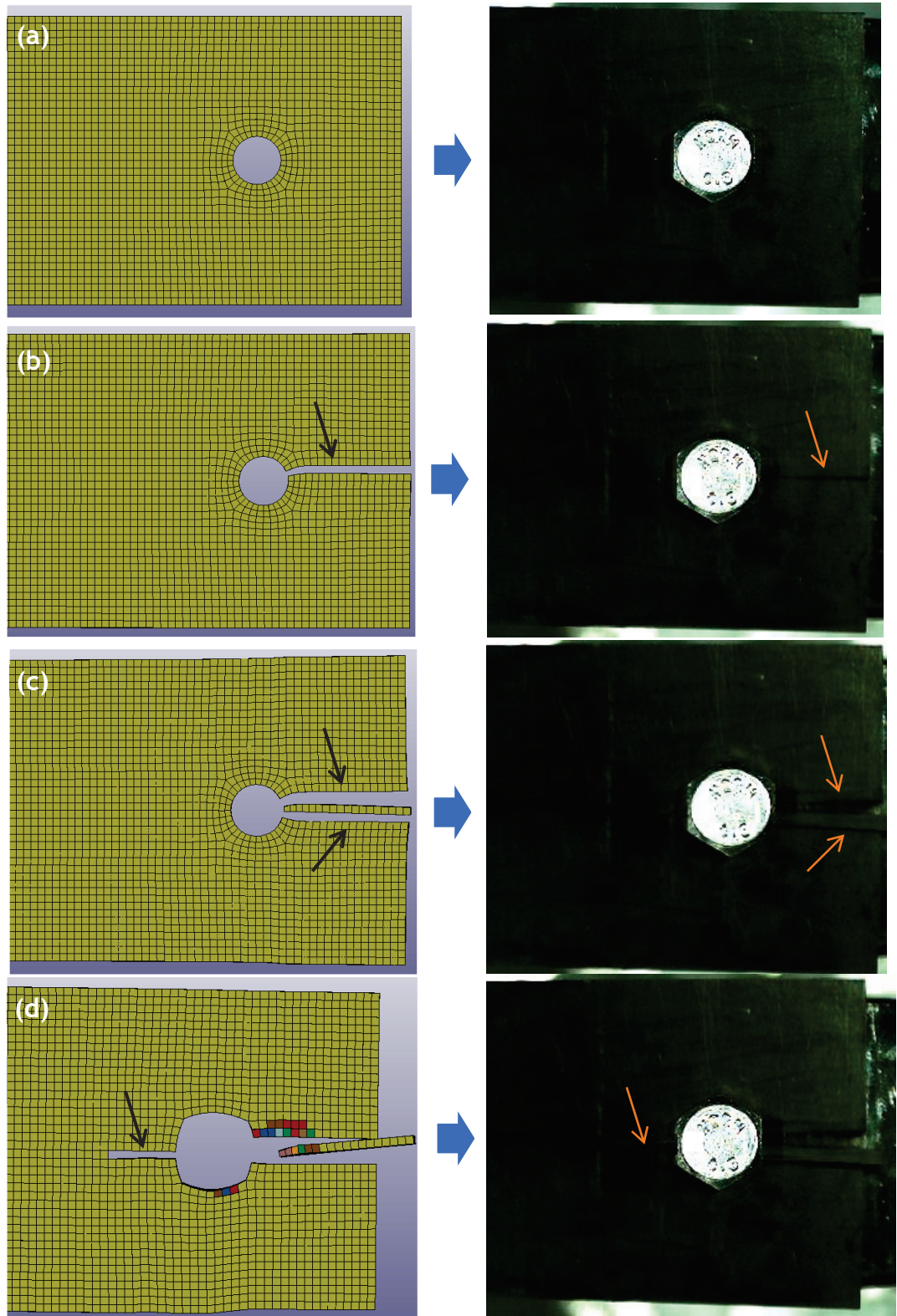


Figure 5.20. Deformation pictures of the pulse implemented dynamic model (a) before crack initiation (b) first crack (c) shear out deformation mode (d) third crack

Perpendicular matrix mode (history variable #10) results of the velocity implemented dynamic model is shown in Figure 5.21(a-c). Figure 5.21(a) clearly indicates the primary deformation mode to be a shear out. After the initiation of the first crack, there was a stress localization in place of the second crack which led the shear out deformation mode (Figure 5.21(b)). Figure 5.21(c) indicates stress localization on the matrix mainly through the side of the specimen. This localization did not result with a failure like the quasi-static model, instead the third crack initiated from the bolt hole through the clamped edge of the specimen. There is no matrix failure spotted around clamp bolts both on tested specimens and models.

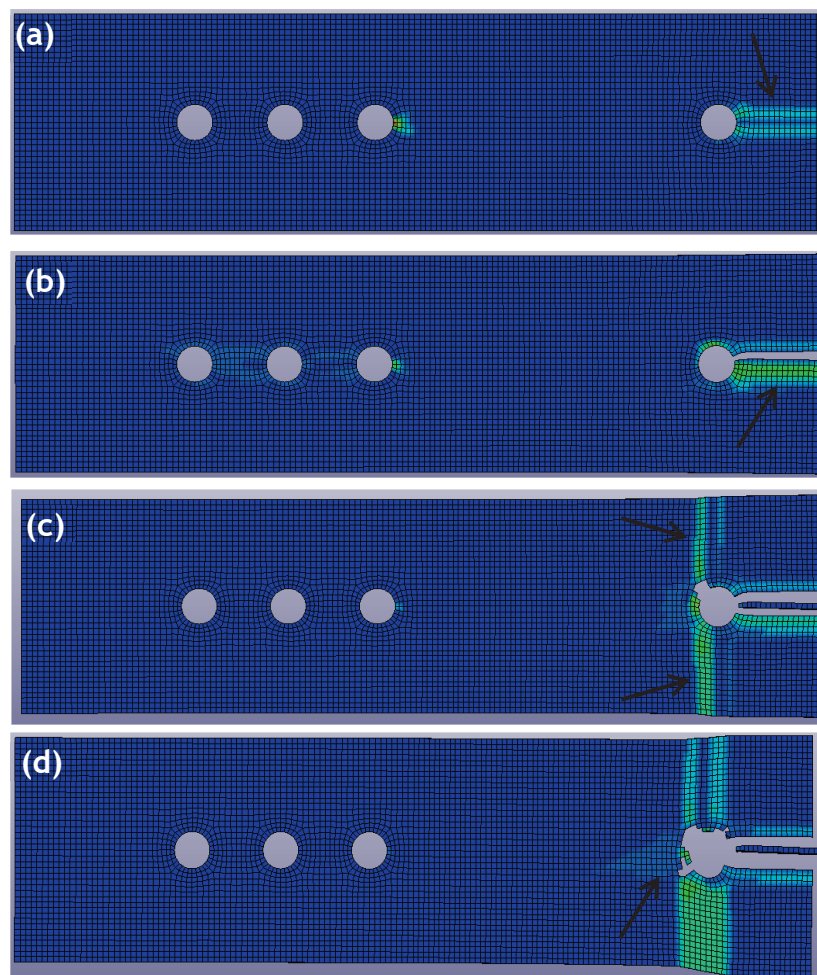


Figure 5.21. Deformation pictures of the velocity implemented model history variable#10 (a) shear-out formation (b) second crack stress localization (c) side stress waves (c) perpendicular stress wave through the fiber direction

CHAPTER 6

CONCLUSION

In this study, mechanical behavior of unidirectional carbon reinforced epoxy bolted composite joints at increasing strain rates at three different loading velocities (3.33×10^{-5} , 1.66×10^{-3} and 12.68 m s^{-1}) has been investigated. Furthermore, two different bolt torques of 2.5 Nm and 10 Nm have been investigated at loading velocities of 3.33×10^{-5} and 12.68 m s^{-1} . ASTM D5961 “bearing response of pinned or fastened joints using multi-directional polymer matrix composite laminates reinforced by high modulus fibers” Procedure C (single-shear tensile loading of one-piece specimen) has been taken into account in order to conduct quasi-static tests. TSHPB has been used in order to conduct the dynamic tests. Two apparatus were designed to provide the same conditions as the ASTM D5961 standard at dynamic tests. The quasi-static and dynamic numerical models have been created using a strain rate dependent material model MAT_162 in order to predict deformation mode and the crack formation forces.

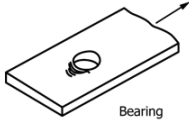
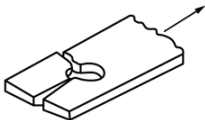
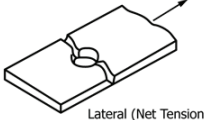
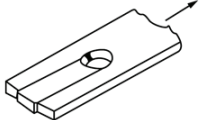
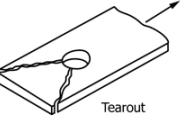











Quasi-static bearing tests were showed two peak forces related to crack formation and two distinct regions at the force-displacement curve. Occurrence of this regions are due to the static frictional forces between the specimen and fixture and the gap between the bolt and the specimen hole. In region i force-displacement curve was showed three various slopes until the specimen fully loaded. In region ii specimen was fully loaded until the deformation. 2.5 and 10 Nm quasi-static tests at $3.33 \times 10^{-5} \text{ m s}^{-1}$ were showed 7% increased first peak force but showed almost no effect on second peak force with an increasing bolt torque. Deformation mode of this tested specimens were determined as cleavage which the first crack starts at a location where the bolt shank contacts with the specimen’s hole and the second crack is formed at the opposite side of the bolt shank’s contact surface and proceeds slowly with increasing load. Quasi-static $1.66 \times 10^{-3} \text{ m s}^{-1}$ velocity tests were showed almost no difference in terms of first and second peak force compared to tests at $3.33 \times 10^{-5} \text{ m s}^{-1}$. Two specimens were failed with the cleavage deformation mode but one specimen was failed with shear-out deformation mode.

Dynamic tests at 12.68 m s^{-1} with 2.5 Nm bolt torque showed 51% increment at the bearing force compared to tests at $3.33 \times 10^{-5} \text{ m s}^{-1}$ with the same bolt torque. With the increase of the loading rate, deformation mode also changed cleavage to shear-out. 2.5 and 10 Nm dynamic tests at 12.68 m s^{-1} were showed 4.5% increased bearing force with an increasing bolt torque. Deformation mode of the 10 Nm dynamic tests determined as cleavage. Quasi-static model was successfully predicted the first peak force and corresponding first crack formation but failed to predict the final deformation mode and related second peak force. The velocity implemented dynamic model is well agreed with the corresponding tests and successfully predicted the final deformation mode and the bearing force. The pulse implemented dynamic model was successfully predicted the deformation mode but failed to predict the bearing force.

The results of this study showed that for [0] dominant composite specimens, increasing loading velocity is very effective on the deformation mode. The change in bolt torque at quasi-static loading velocity was slightly effective on peak forces however at dynamic loading velocities bolt torque drastically changed the deformation mode.

APPENDIX A

BEARING TEST FAILURE CODES WITH ILLUSTRATIONS OF COMMON MODES

					
B1I	C1I	L1I	S1I		
					
T1I	D1I	P1B	Y3H		
					
Y3N	Y3T	E3H	E3S		
					
T3H	T3T	S3S	S3T		
First Part		Second Part		Third Part	
Failure Type	Code	Failure Area	Code	Failure Location	Code
Laminate Bearing	B	1 st Hole	1	Laminate Head Side	B
Laminate Cleavage	C	2 nd Hole	2	Laminate Nut Side	N
Laminate (lateral) Net Tension	L	Both Holes	B	Fastener Head	H
Laminate Shear-Out	S	1 st Fastener	3	Fastener Nut/Collar	C
Laminate Tear-Out	T	2 nd Fastener	4	Fastener Shank	S
Laminate Delamination	D	Both Fasteners	F	Fastener Thread	T
Laminate Pull-Through	P			Inapplicable	I
Fastener Yield	Y			Unknown	U
Fastener Bending	E				
Fastener Tension	F				
Fastener Shear	G				
Multi-Mode	M(xyz)				
Other	O				

(D5961/D5961M – 17 Standard Test Method for Bearing Response of Polymer Matrix Composite Laminates)

REFERENCES

1. Khashaba, U. A.; Sallam, H. E. M.; Al-Shorbagy, A. E.; Seif, M. A., Effect of washer size and tightening torque on the performance of bolted joints in composite structures. *Composite Structures* **2006**, *73* (3), 310-317.
2. Sen, F.; Pakdil, M.; Sayman, O.; Benli, S., Experimental failure analysis of mechanically fastened joints with clearance in composite laminates under preload. *Materials & Design* **2008**, *29* (6), 1159-1169.
3. Yazdani Nezhad, H.; Egan, B.; Merwick, F.; McCarthy, C. T., Bearing damage characteristics of fibre-reinforced countersunk composite bolted joints subjected to quasi-static shear loading. *Composite Structures* **2017**, *166*, 184-192.
4. Kweon, J.-H.; Jung, J.-W.; Kim, T.-H.; Choi, J.-H.; Kim, D.-H., Failure of carbon composite-to-aluminum joints with combined mechanical fastening and adhesive bonding. *Composite Structures* **2006**, *75* (1), 192-198.
5. Gomez, L.; Olivares, G.; kona ravi, A.; Bhasin, A.; Gomez, A.; Keshavanarayana, S.; Pang, J.; Molitor, M.; Rassaian, M., *Evaluation of Ls-Dyna MAT162 for Modeling Composite Fastener Joints for High Rates of Loading*. 2019.
6. Tserpes, K. I.; Papanikos, P.; Kermanidis, T. H., A three-dimensional progressive damage model for bolted joints in composite laminates subjected to tensile loading. *Fatigue & Fracture of Engineering Materials & Structures* **2001**, *24* (10), 663-675.
7. Hashin, Z., Failure Criteria for Unidirectional Fiber Composites. *Journal of Applied Mechanics* **1980**, *47* (2), 329-334.
8. Poon, C.; Shokrieh, M.; Lessard, L., Three-Dimensional Progressive Failure Analysis of Pin/Bolt Loaded Composite Laminates. **1996**.

9. Zhou, Y.; Yazdani-Nezhad, H.; McCarthy, M. A.; Wan, X.; McCarthy, C., A study of intra-laminar damage in double-lap, multi-bolt, composite joints with variable clearance using continuum damage mechanics. *Composite Structures* **2014**, *116*, 441-452.
10. Heimbs, S.; Hoffmann, M.; Waimer, M.; Schmeer, S.; Blaurock, J., Dynamic testing and modelling of composite fuselage frames and fasteners for aircraft crash simulations. *International Journal of Crashworthiness* **2013**, *18*, 406-422.
11. Pearce, G. M. K.; Johnson, A. F.; Hellier, A. K.; Thomson, R. S., A study of dynamic pull-through failure of composite bolted joints using the stacked-shell finite element approach. *Composite Structures* **2014**, *118*, 86-93.
12. Liu, L.; Zhang, J.; Chen, K.; Wang, H., Combined and interactive effects of interference fit and preloads on composite joints. *Chinese Journal of Aeronautics* **2014**, *27* (3), 716-729.
13. Egan, B.; McCarthy, C. T.; McCarthy, M. A.; Gray, P. J.; Frizzell, R. M., Modelling a single-bolt countersunk composite joint using implicit and explicit finite element analysis. *Computational Materials Science* **2012**, *64*, 203-208.
14. Zhou, Y.; Yazdani Nezhad, H.; Hou, C.; Wan, X.; McCarthy, C. T.; McCarthy, M. A., A three dimensional implicit finite element damage model and its application to single-lap multi-bolt composite joints with variable clearance. *Composite Structures* **2015**, *131*, 1060-1072.
15. Puck, A.; Schürmann, H., Failure analysis of FRP laminates by means of physically based phenomenological models. *Composites Science and Technology* **2002**, *62* (12), 1633-1662.
16. McCarthy, C.; McCarthy, M.; Stanley, W.; Lawlor, V., Experiences with Modeling Friction in Composite Bolted Joints. *Journal of Composite Materials - J COMPOS MATER* **2005**, *39*, 1881-1908.

17. Heimbs, S.; Schmeer, S.; Blaurock, J.; Steeger, S., Static and dynamic failure behaviour of bolted joints in carbon fibre composites. *Composites Part A: Applied Science and Manufacturing* **2013**, *47*, 91-101.
18. Portemont, G.; Berthe, J.; Deudon, A.; Irisarri, F.-X., Static and dynamic bearing failure of carbon/epoxy composite joints. *Composite Structures* **2018**, *204*, 131-141.
19. Li, Q. M.; Mines, R. A. W.; Birch, R. S., Static and dynamic behaviour of composite riveted joints in tension. *International Journal of Mechanical Sciences* **2001**, *43* (7), 1591-1610.
20. Pearce, G.; Johnson, A.; Thomson, R.; Kelly, D., Experimental Investigation of Dynamically Loaded Bolted Joints in Carbon Fibre Composite Structures. *Applied Composite Materials* **2010**, *17*, 271-291.
21. Heimbs, S.; Bergmann, T., Bearing Mode Absorber – On the Energy Absorption Capability of Pulling a Bolt through a Composite or Sandwich Plate. *Procedia Engineering* **2014**, *88*, 149-156.
22. Ger, G. S.; Kawata, K.; Itabashi, M., Dynamic tensile strength of composite laminate joints fastened mechanically. *Theoretical and Applied Fracture Mechanics* **1996**, *24* (2), 147-155.
23. Egan, B.; McCarthy, C. T.; McCarthy, M. A.; Gray, P. J.; O'Higgins, R. M., Static and high-rate loading of single and multi-bolt carbon–epoxy aircraft fuselage joints. *Composites Part A: Applied Science and Manufacturing* **2013**, *53*, 97-108.
24. Wang, P.; Chen, H.-s.; Zhu, X.; zhao, Q.; Fang, D., A novel predictive model for mechanical behavior of single-lap GFRP composite bolted joint under static and dynamic loading. *Composites Part B: Engineering* **2015**, *79*.
25. VanderKlok, A.; Dutta, A.; Tekalur, S. A., Metal to composite bolted joint behavior evaluated at impact rates of loading. *Composite Structures* **2013**, *106*, 446-452.

26. Kwon, J.; Choi, J.; Huh, H.; Lee, J., Evaluation of the effect of the strain rate on the tensile properties of carbon-epoxy composite laminates. *Journal of Composite Materials* **2016**, *0*.
27. McCarthy, M. A.; Lawlor, V. P.; Stanley, W. F.; McCarthy, C. T., Bolt-hole clearance effects and strength criteria in single-bolt, single-lap, composite bolted joints. *Composites Science and Technology* **2002**, *62* (10), 1415-1431.
28. Matzenmiller, A.; Lubliner, J.; Taylor, R. L., A constitutive model for anisotropic damage in fiber-composites. *Mechanics of Materials* **1995**, *20* (2), 125-152.
29. Lee, S.; Byun, J.; Cho, H. In *Progressive damage structural analysis of carbon/epoxy composite laminates*, The 18th International Conference of Composite Materials, ICC Jeju, Korea, 2011; pp 21-26.